2020

Space Weathering Simulation Trends on Carbonaceous Chondrites

Andrew Malfavon
University of Central Florida

SPACE WEATHERING SIMULATION TRENDS ON CARBONACEOUS CHONDRITES

by

ANDREW MALFAVON
B.S Chapman University, 2016

A thesis submitted in partial fulfilment of the requirements
for the degree of Master of Science
in the Department of Physics
in the College of Sciences
at the University of Central Florida
Orlando, Florida

Fall Term
2020

Major Professor: Humberto Campins

ABSTRACT

Space weathering on primitive asteroids is an ongoing area of research. Primitive asteroids have low geometric albedo ($\leq$ 0.15) and mostly featureless visible spectra ($\sim$0.5 - 0.9 μm) (Campins et al. 2018). Higher albedo S-type asteroids and their corresponding meteorites, ordinary chondrites, have well-characterized space weathering effects. The generally lower albedo primitive asteroids and their less common corresponding meteorites, carbonaceous chondrites, have shown various, sometimes disagreeing results in laboratory simulations. Experiments simulating solar wind exposure on carbonaceous chondrites by Lantz et al. (2017) and Nakamura et al. 2019 showed complex trends on different types of meteorite samples. Thompson et al. (2019) simulated micrometeorite impacts on CM meteorites. Results from the Japanese sample return mission Hayabusa2 to asteroid Ryugu show an agreement with trends found by both Thompson et al. (2019) and Nakamura et al. (2019). Here, I investigate various laboratory simulations of carbonaceous chondrites to determine if certain experimental conditions were leading to disagreeing results. The two main differences I analyzed were the preparation of the sample (powder or pellet or chip) and type of space weathering being simulated (solar wind or micrometeorite bombardment). My analysis shows no clear trend for these space weathering results, suggesting the experiments on carbonaceous chondrites may not be accurately representing what is happening to their primitive asteroid counterparts.

TABLE OF CONTENTS

LIST OF FIGURES

LIST OF TABLES

CHAPTER 1: INTRODUCTION

Asteroids are believed to be remnants of the early Solar System formation with low albedo, mostly featureless primitive asteroids especially serving as a record of the original composition of the solar nebula. Understanding the collisional and dynamical processes that formed and changed asteroids can reveal clues to Solar System formation. Over time, asteroid spectra may change due to various processes, such as impacts and exposure to solar rays. A clear understanding of these changes is necessary to understand how they relate to Solar System Formation.

Classification of asteroids and meteorites resulted in a mismatch of asteroid type to corresponding meteorite type. The Tholen classification system (Tholen 1984) uses visible (VIS; $\sim$0.5 - 0.9 μm) and near-infrared (NIR; 0.8 - 2.5 μm) spectra to categorize asteroids and determine their surface mineralogy. S-types (named for a 0.95 μm band interpreted to be due to silicate minerals) (Chapman et al. 1975) are the most common asteroid type in the inner half of the asteroid belt, yet their spectra does not match with that of the most common meteorite, ordinary chondrites (contain a mixture of the minerals olivine and pyroxen) (Burbine et al. 2003). Some form of alteration process was suspected to be the cause for this discrepancy. Moon samples confirmed exposure to space can cause surfaces to change over time (Conel & Nash, 1970). Various laboratory simulations combined with direct evidence from the Hayabusa mission of asteroid Itokawa created a general trend for what is known as space weathering (Noguchi et al. 2011).

Space weathering is the alteration of the surface of airless bodies due to bombardment of solar wind particles and micrometeoroids. The remotely sensed properties of asteroid bodies can be modified through space weathering from the intrinsic properties of the bulk of the body, leading to confused interpretations of telescopic spectra of asteroids (Chapman 2004). Sample return missions to asteroids provide important data on composition of the body, however, Earth-based telescopic observations are necessary to extrapolate this data to the entire asteroid population.

Laboratory simulations on meteorite samples have been used as a method to better under-

stand processes and alterations from space weathering. S-type asteroids now have well understood outcomes from space weathering, however there is disagreement between simulations on carbonaceous chondrites, which are meteorites believed to come from primitive asteroids. Carbonaceous chondrites have a composition of Ca-Al-rich inclusion, Fe-Ni-metal, mostly silicate chondrules, and a fine-grained matrix of organic matter (Lantz et al. 2017; Lauretta et al. 2006; Pizzarello et al. 2006). Primitive asteroids are of great interest in sample return missions, such as the on-going OSIRIS-REx and Hayabusa2 missions. They present clues to the evolution of our Solar System and can be potentially hazardous to humans or used as resources. Some have orbits which may evolve to become a threat to Earth. They are also near enough to possibly serve as a source of fuel and building materials for space missions in the future, allowing for more efficient launches (Campins et al. 2018).

1.1 Lunar space weathering

Studies into how processes, such as meteorite impacts and erosion, may be altering optical properties of the lunar surface date back to the 1950s and 1960s (Gold, 1955; Shoemaker, 1962). Ion bombardment from solar wind was suggested by Hapke (1962) as a possible altering process for the lunar surface. In order to test this theory ahead of future lunar missions, Hapke (1965) conducted the first space weathering laboratory simulations. Powders with an average particle size of 10 μm were made from samples of biotite granite, tektite, basalt, and dunite (Hapke, 1965). The powders were irradiated with hydrogen ions with an energy level of 2 keV over a time sufficient to deposit an electric flux density of the order of 100 $\mathrm{coulombs/cm^2}$ (Hapke, 1965). These values were calculated to represent irradiation of about 2×10^5 years on the moon. Spectral measurements before and after the simulation show a darker albedo and a redder spectral slope (the reflectance is increasing with increasing wavelength) in the visible range, matching more closely with telescopic lunar spectra (Hapke, 1968). Basalt matched most closely with lunar spectra, lead-

ing Hapke (1968) to conclude the lunar surface is likely composed of iron-rich basalts rather than ordinary chondrites, a popular hypothesis at the time. Hapke (1965) notes other factors may be contributing to lunar space weathering in addition to solar wind. Micrometeorite bombardments exposing fresh, less-weathered material may explain why some of the experiments result in albedo darker than lunar albedo (Hapke, 1965). Although these early experiments resulted in correct conclusions (lunar regolith composition, processes leading to lunar space weathering, and the general trend in the spectral alteration), hindsight shows the experimental issues, such as contamination and an oversimplification of the space weathering process, means this is not a complete picture of space weathering (Chapman, 2004).

Direct evidence of space weathering on the Moon was found in the 1970s by comparing Apollo lunar samples to telescopic reflectance data of the collection sites (Hapke et al. 1975). Apollo 11 lunar soil samples were compared to synthetic glass made from the same samples to determine how reflectance spectra of lunar samples differed from pristine rocks/minerals of the same composition (Conel & Nash, 1970). The soils had different spectral properties in the VIS and NIR than the larger fragments, including a redder spectral slope, a darker albedo, and weaker absorption bands. These spectral changes are shown in Figure 1.1 with the mature soil being more weathered than the rock fragments (Adams & Jones, 1970). Solar wind bombardment on the lunar surface produces nanophase metallic iron (Keller & McKay, 1997), which causes a more red-sloped reflectance spectra, darker visible-near-infrared (VNIR; 0.5 - 2.5 μm) spectrum, and a weakening of absorption features (Adams & McCord, 1970). Micrometeorite impacts can cause shock, melting, and vaporization of grains, as well as burial of the surface material and excavation of buried materials (McKay et al. 1991). Since these discoveries, the Moon has become the main source of space weathering research.

Space weathering on lunar regolith cause lunar soil grains to become surrounded by 60 – 200 nm size rims of varying chemical compositions (Keller & McKay, 1997). One major form of these rims, called inclusion-rich rims by Keller & McKay (1997), are characterized by submi-

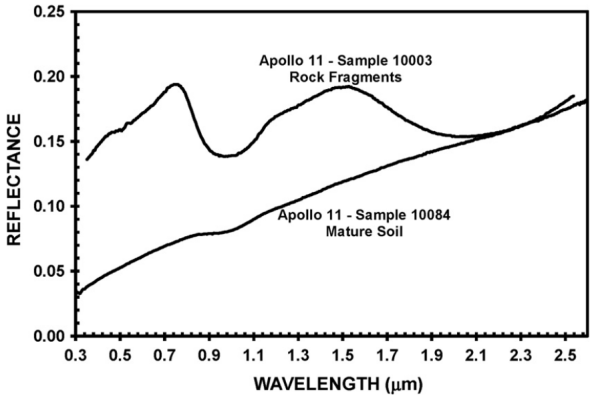

Figure 1.1: Spectra of mature lunar soil and less space weathered lunar rock fragments from the Apollo 11 mission. The soil shows the characteristic reddened slope, lower overall reflectance, and weakened absorption features for lunar regolith.(Reprinted from Gaffey et al. (2010), with permission from Elsevier; based on data from Adams & Jones (1970). Reprinted with permission from AAAS.)

crometer crystalline inclusions of Fe-metal. Keller & McKay (1997) predicted inclusion-rich rims on lunar soil to be the main source of optical changes from space weathering. Results from Pieters et al. (1993) and Allen et al. (1996) support this claim by showing Fe metal grains must be 10 nm for significant reddening of the slope to occur. Large ($\sim$2 μm; Britt, 1991) Fe grains cause a darkening without a reddening. Since lunar soil shows both darkening and reddening, vapor-deposited coatings containing submicroscopic Fe-metals must be coating the lunar soil over time.

The production of nanophase reduced iron through vapor deposition and irradiation was shown by Pieters et al. (2000) to be the product of space weathering in lunar soils as well as in S-type asteroids. They showed nanophase iron particles occurred from both ion-particle sputtering and from micrometeorite impacts. Pieters et al. (2000) also showed a correlation in optical trend to total amount of nanophase iron. The amount of nanophase iron is in turn correlated to the amount of Fe in the host material, the flux and energy of micrometeorite bombardment, the flux of solar ion irradiation, and the time of exposure (Pieters et al. 2000). This process is extended to S-type asteroids as a way to explain the connection between S-type asteroids and ordinary chondrites as

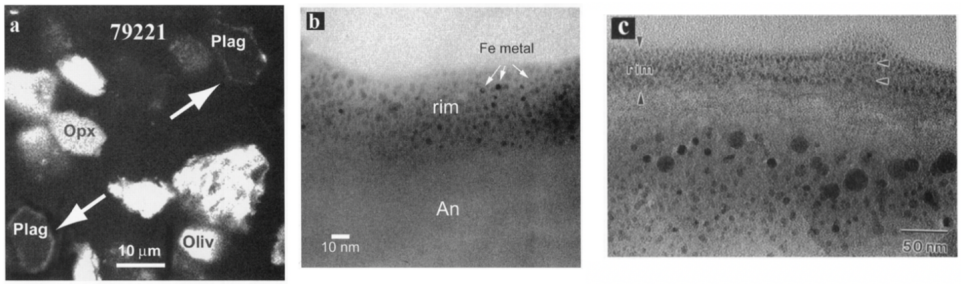

Figure 1.2: (a) X-ray Fe Kα image of lunar soil sample 79221, which is sensitive to Fe, showing an enrichment of iron around the plagioclase grain. (b) A transmission electron microscope image of lunar soil sample 79221, with dark circles representing nanophase iron particles that form a rim on a grain of plagioclase anorthosite. (c) A transmission electron microscope image of lunar soil sample 79221 with different sized nanophase iron particles showing up as dark circles. The size difference corresponds to different amounts of space weathering. (From Pieters et al. (2000), with permission from John Wiley and Sons.)

their parent bodies. Pieters et al. (2000) suggest the accumulation of nanophase iron particles may be a natural result of space weathering on semi-transparent minerals, and since C-type asteroids are optically opaque, this process may not apply to them.

Figure 1.2a from Pieters et al. (2000) shows an X-ray Fe Kα of lunar soil sample 79221. This X-ray is sensitive to the amount of iron present in the sample. In Figure 1.2a, the arrow indicates a plagioclase grain with an Fe enhanced rim. Figure 1.2b and 1.2c both show transmission electron microscope images. 1.2b is of a plagioclase grain from soil sample 79221, and 1.2c is of a lunar agglutinate. Both images show layers of nanophase iron, represented by the dark circles. The size of the particles produced will have a direct influence on the spectral darkening and reddening of the soil. Reflectance spectra of the lunar soil samples 10084 and 62231 compared with lunar basalt chips (10003) over $\sim$0.45-2.5 μm shows drastic difference in absorption bands (Pieters et al. 2000). The lunar basalt chip shows prominent high-Ca pyroxene absorptions near 1.0 and 2.2 μm, while both lunar soils are steeper with little to no absorption bands at the same wavelengths. Build-up of nanophase iron particles results in a loss of spectral contrast of absorption features.

Understanding of space weathering began with studies of lunar soil, however there are major differences between effects on the Moon and on asteroids. Since solar wind is a major component of space weathering, distance from the sun has a large influence on the effects. Meteorite impacts on asteroids happen at much lower velocities than on the Moon (Hapke et al. 2001), suggesting the second major component of space weathering, micrometeorite impacts, is also different on asteroid surfaces. Compositional differences of the target bodies change the effect of space weathering as well, meaning it is much more difficult to make a simple analogy between lunar surface alteration and asteroid surface alteration.

1.2 Asteroid space weathering

Initial attempts to understand space weathering on asteroids had to rely on telescopic observations and laboratory simulations on meteorite samples. Results from these experiments and observations would later be confirmed by space missions. Laboratory simulations focused on replicating the two main space weathering processes: solar wind and micrometeorite bombardment.

Solar wind and cosmic rays produce the ions believed to be the main radiation driver of space weathering on airless bodies (Keller & McKay, 1997). More than 99% of solar wind is hydrogen and helium ions, which have a mean energy of 1 keV per atomic mass unit (Gosling, 2007). Cosmic rays consist mostly of hydrogen ions with a lower flux than solar wind, but with more energy, allowing them to penetrate deeper into the surface of the body. Ions interacting with mineral samples can alter their surface by transferring energy as they travel through the grain. Sputtering, structural, and chemical changes may occur with varying degree depending on the stopping power of the ions. Energy transfer within atoms in the solid occur through inelastic, electronic collisions or elastic, nuclear collisions. The two different forms of energy transfer produce alterations in the sample, thus contributing to space weathering effects by creating nanoparticles which alter the VNIR spectra (Hapke et al. 1975).

Micrometeorite bombardment (some of which travel kilometers per second) collide with

asteroid surfaces and slow down quickly enough to vaporize surface grains (Adams & McCord, 1971). Micrometeorite impacts are easily simulated using pulsed lasers at fluences higher than the ablation threshold. These pulses can quickly deposit large amounts of energy, $10^{-3} - 1\ J/\mathrm{cm}^2$ (Kissel & Krueger, 1987), although the energy is not more than the equivalent of an impact by a dust particle with $\sim$10 μm diameter. A more direct recreation of micrometeorite bombardment is through dust accelerators, such as the 3 MV hypervelocity dust accelerator at the Colorado Center for Lunar Dust and Atmorspheric Studies (Shu et al. 2012). This machine can emit single particles of a specific mass and velocity in a much more controlled manner than the more common pulsed lasers, however, these types of machines are expensive and very specialized (Shu et al. 2012).

In order to replicate the large timescales asteroids experience space weathering, the total fluence (ions per square centimeter) must be considered instead of the flux (ions per square centimeter per second). Ion currents that do not cause macroscopic heating are used in laboratory experiments to simulate long time-scale micrometeorite bombardment. A qualitative comparison of energy deposited by fast impacts with energy deposited by lasers is necessary as surface mineral vaporization is nonlinear (e.g., Sasaki et al. 2001).

S-type asteroids and their corresponding meteorites, ordinary chondrites, were the first objects targeted to replicate the process used to understand lunar space weathering. S-type asteroids are more easily observed because of their high albedo and absorption bands (Lantz et al. 2013). They are the most common asteroid type in the inner half of the asteroid belt and ordinary chondrites are the most common meteorite (Chapman et al. 1975). The early studies of space weathering on the lunar surface were connected to the ordinary chondrite material that make up the S-type asteroids, since the Moon and S-type asteroids are both made up of primarily silicates (Adams & McCord, 1971). Space weathering simulations on ordinary chondrites were able to alter the spectra of the samples to better match telescopic spectra of S-type asteroids (Clark et al. 1992). Lowering of albedo and reddening of slope is the accepted space weathering trend for silicates. The darkening/reddening trend was then confirmed with space missions to S-type asteroids 433

Eros (e.g., Clark et al. 2001) and 25143 Itokawa (e.g., Ishigura et al. 2007).

The production of nanoparticles due to space weathering processes creates the optical changes seen in materials (Hapke et al. 1975). For lunar regolith, S-type asteroids, and ordinary chondrite meteorites, nanophase reduced iron is the main product of space weathering processes (Clark et al. 2002). Thompson et al. (2019) analyzed the products from their space weathering experiments on carbonaceous chondrites (discussed in detail in section 3.3), however, this is less studied than the products formed on ordinary chondrites. The process of comparing laboratory simulations to telescopic observations proves to be more complicated for primitive asteroids and carbonaceous chondrites.

CHAPTER 2: SPECTRAL CHANGES OF ASTEROIDS AND METEORITES

Space weathering effects (spectral reddening, reflectance darkening, and a shift in the 1 and 2 μm absorption band) in the visible-near-infrared (VNIR; 0.4-2.5μm) region are well known for silicate-rich asteroids (S-type) due to a large observational data set. Analysis of spectra of S-type asteroids in the main belt and near-Earth populations, as well as ordinary chondrite meteorites, shows a similar mineralogy but the slopes do not match. Many meteorites likely originated from near-Earth asteroids, since they are the closest source. Marchi et al. (2005) analyzed VNIR spectra of main belt S-types and a significant number of near-Earth asteroids to explore their connection to ordinary chondrites. They compared the observational spectra to the laboratory spectra of ordinary chondrite meteorites because these are believed to be the best analogues to S-type asteroids. Marchi et al. (2005) conducted solar wind simulations on these samples by performing ion irradiation experiments.

Spectral slopes for the main belt asteroids, near-Earth asteroids, and ordinary chondrites analyzed by Marchi et al. (2005) were computed from a fitted continuum across absorption band near 1 μm, based on the parameters from Gaffey et al. (1993). Comparison of observational data to known laboratory spectra of ordinary chondrites shows 95% of ordinary chondrites have a spectral slope across the 1 μm absorption band that lies below 83% of the near-Earth asteroids and 94% of the main belt asteroids (Marchi et al. 2005). The discrepancy seems to be resolved when meteorite samples are irradiated. After irradiation, the spectral slope across the band near 1 μm becomes redder, better matching the spectral slope of the S-types also across the band near 1 μm. Figure 2.1 shows reflectance spectra of three ordinary chondrites before and after irradiation (Marchi et al. 2005). These samples start with a slope below the ordinary chondrite limit, and a slope above the limit as they experience irradiation. The samples are reddening to more closely match the observed

slopes of near-Earth and main belt objects. Figure 2.2 from Marchi et al. (2005) shows the initial discrepancy between the spectra of ordinary chondrites and S-types and how, after irradiation, the slope of the ordinary chondrites shift to match the S-types. There is a spectral slope value (0.138 μm^{-1}) which is higher than 95% of the spectral slope for ordinary chondrites. Based on the irradiation experiments on the ordinary chondrites (Marchi et al. 2005), S-types with spectral slopes above the 0.138 μm^{-1} are considered weathered. This is about 83% of near-Earth asteroids and 94% of main belt asteroids (Marchi et al. 2005).

Ordinary chondrite-like objects have been the most studied despite making up a relatively small portion of the asteroid belt. About half of the main-belt objects are considered primitive, which are carbonaceous chondrite-like, yet only about 5% of meteorites are carbonaceous chondrites (Lantz et al. 2015b). Primitive objects have low albedo (≤ 0.15), mostly featureless spectra, and belong to the C-complex in the Tholen classification system (contains B, C, D, F, G, and T-types) (Tholen & Barucci, 1989; Campins et al. 2018). The discrepancy between the number of C-complex asteroids and the amount of their corresponding meteorites may be due to a bias in meteorite collection. Certain areas on Earth have a high accumulation rate of meteorites, possibly due to periods of time when meteorite fall rate was significantly greater than today (Zolensky et al. 1990). Since meteorite collectors know these areas have a large quantity of meteorites, these are the locations they will search, leading to a high collection of the same type of meteorites. The low albedo of primitive asteroids make them more difficult to observe from Earth, leading to less observations to compare to carbonaceous chondrite spectra. Less observations of primitive asteroids with respect to S-types and the small sample of carbonaceous chondrites both contribute to the lack of conclusive space weathering trends for C-complex asteroids.

2.1 Absorption Bands

Ordinary chondrites and S-type asteroids experience weakening of diagnostic spectral fea-

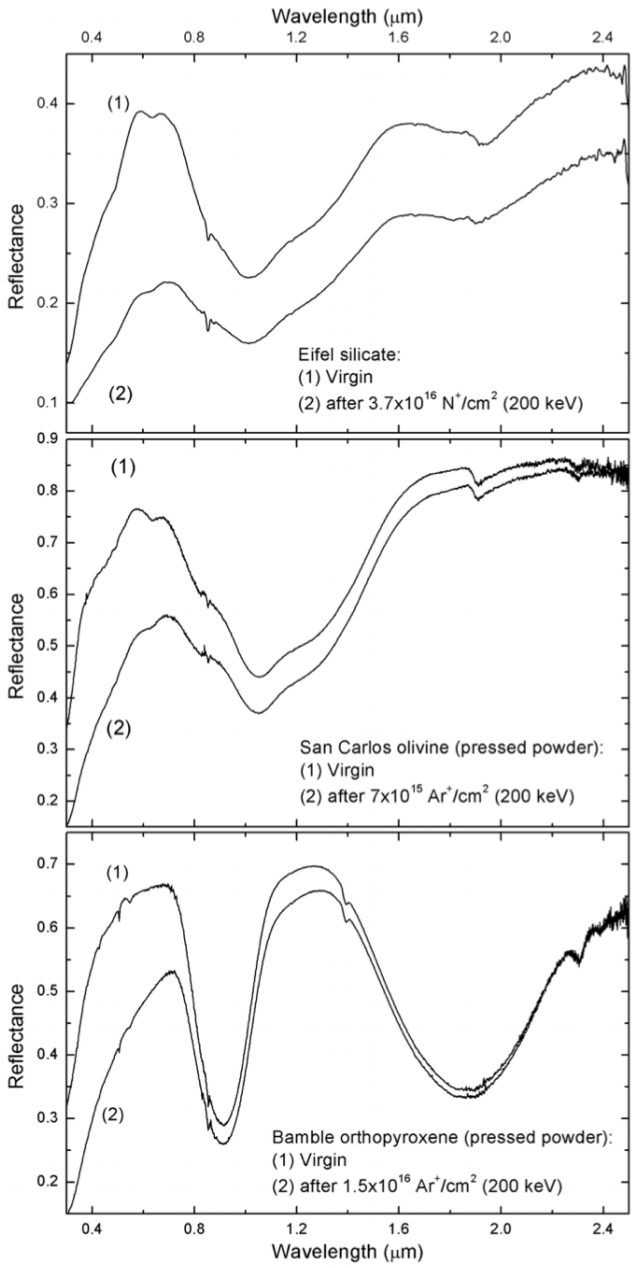

Figure 2.1: Reflectance spectra of three ordinary chondrites before and after irradiation. There is an absorption band feature near 1 μm. A fitted continuum across this band is used to determine the spectral slope, which becomes redder after irradiation. Reflectance also gets lower. (Credit: Marchi et al. (2005), reproduced with permission © ESO.)

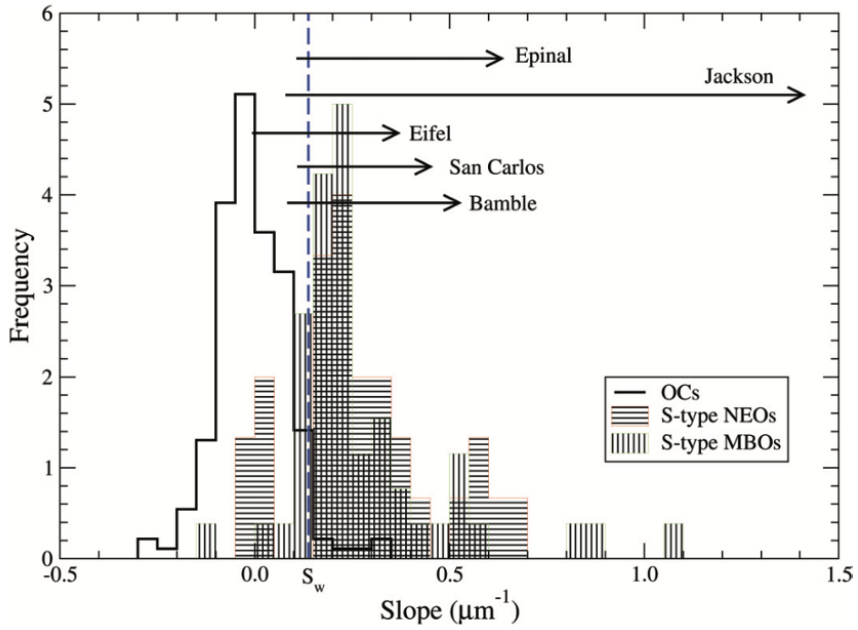

Figure 2.2: Spectra of ordinary chondrites and their corresponding S-type asteroids have slopes that originally do not match up, but after irradiation, the spectral slopes of the ordinary chondrites shift to better line up with the spectral slopes of the S-types.(Credit: Marchi et al. (2005), reproduced with permission © ESO.)

tures in the VNIR. Absorption bands for S-type asteroids and ordinary chondrites are consistent with mixtures of olivine and/or pyroxene, however, asteroids have shallower bands than meteorites (Burbine, 2016), suggesting space weathering on S-type asteroids also cause a weakening of absorption bands. Figure 2.3 shows three ordinary chondrites with clear absorption bands near 1 μm and 2 μm. Comparison with spectra of S-complex asteroids from the Bus-DeMeo asteroid taxonomy (DeMeo et al. 2009) shows similar locations of absorption bands, however they are noticeably weaker.

Primitive asteroids have relatively few VNIR spectral features compared to S-complex, all relating to hydrated minerals (Campins et al. 2018). A prominent 0.7 μm feature attributed to phyllosilicates (Vilas & Gaffey, 1989) was found in the Erigone asteroid family, for 86.6% of C-types, 28.6% of X-types, 36.4% of B-types, and 14.3% of T-types (Morate et al. 2016). Another

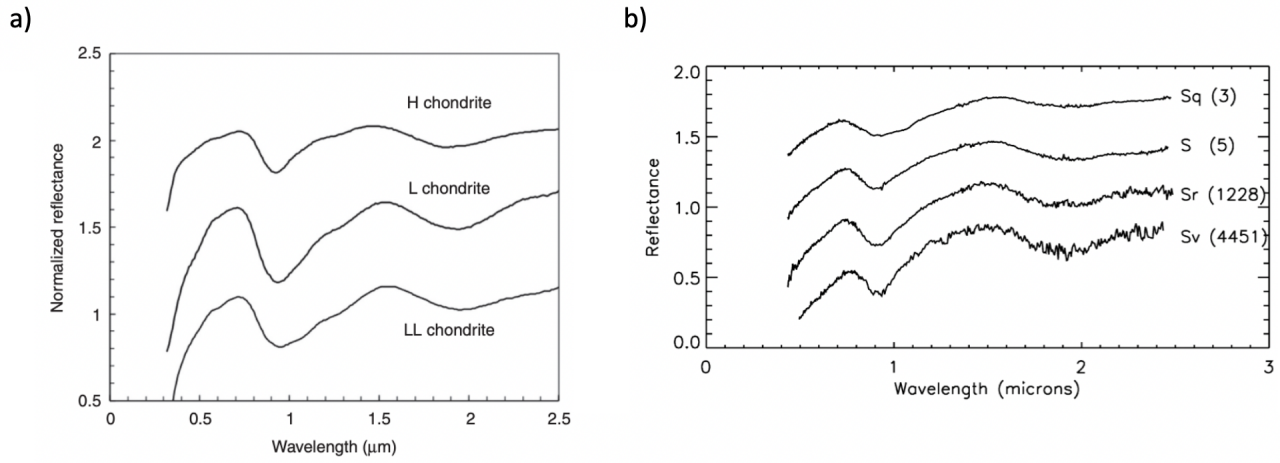

Figure 2.3: (a) Spectra of three ordinary chondrite meteorites, showing absorption bands near 1 μm and 2 μm.(From Burbine (2016), © ESO 2005, reproduced with permission of the Licensor through PLSclear. Based on data from Burbine et al. (2003)) (b) Spectra of objects within the S-complex asteroid taxonomy. They show absorption bands near 1 μm and 2 μm, however, the bands are weaker than their meteorite analogues. (Reprinted from DeMeo et al. (2009) with permission from Elsevier.)

observational study by Fornasier et al. (2014) found 50% of C-types and all G-types to have this feature.

A more diagnostic feature of hydrated asteroids due to the symmetric and asymmetric stretches of water molecules (Takir et al. 2018) is the 3 μm region. Although the presence of either a 0.7 μm feature or a 3 μm feature is sufficient to show the existence of hydrated minerals on an asteroid, the 3 μm feature is more sensitive and can be present while a 0.7 μm feature is not (Rivkin et al. 2002). Studies have shown half of observations with a 3 μm feature do not have a 0.7 μm, while the presence of a 0.7 μm feature is always accompanied with a 3 μm (Villas, 1994; Rivkin et al. 2002).

Carbonaceous chondrites have suppressed absorption bands in the visible and near-infrared range, due to the opaques, while phyllosillicates create strong absorptions in the 3 μm region due

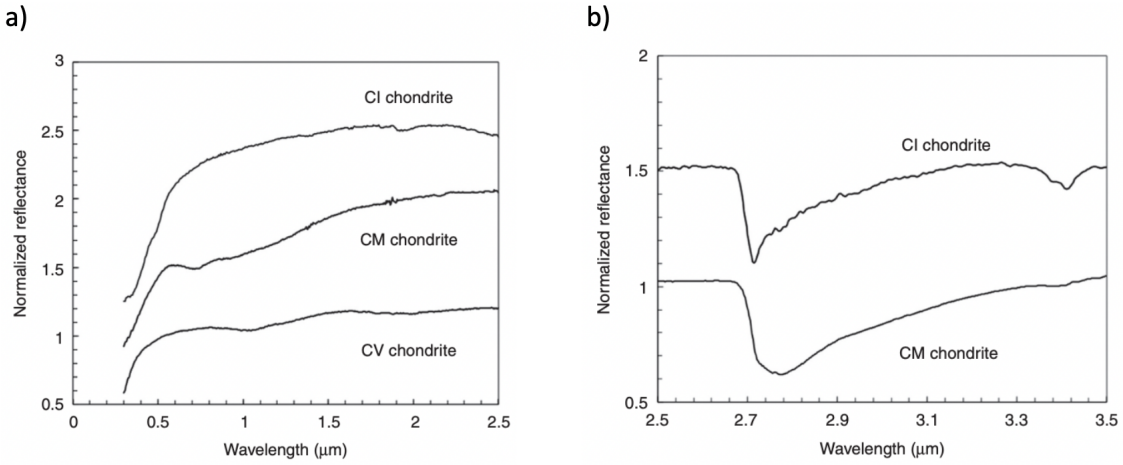

Figure 2.4: (a) Reflectance spectra for three carbonaceous chondrite meteorites show slight absorption bands at $\sim$0.7 μm for the CM and $\sim$1 μm for the CV. (From Burbine (2016), © ESO 2005, reproduced with permission of the Licensor through PLSclear. Based on data from Hiroi et al. (1993) and Sunshine et al. (2008).) (b) Reflectance spectra for two carbonaceous chondrite meteorites with strong absorption bands $\sim$2.7-2.8 μm. (From Burbine (2016), © ESO 2005, reproduced with permission of the Licensor through PLSclear. Based on data from Takir et al. (2013).)

to -OH (Burbine, 2016). Figure 2.5a shows three types of carbonaceous chondrites in the visible to near-infrared region. They are mostly featureless, with a slight absorption band at $\sim$0.7 μm in the CM chondrite and $\sim$1 μm in the CV chondrite. Figure 2.5b shows a CI and CM chondrite in the 2.5 to 3.5 μm region, displaying strong absorption bands between 2.7-2.8 μm. This shows the benefit of the 3 μm region for lower albedo, often featureless objects such as primitive asteroids and carbonaceous chondrites.

Experiments on carbonaceous chondrites to replicate space weathering effects have shown absorption bands to "shift" toward longer wavelengths (Lantz et al. 2017) however, this shift is only clear in the longer wavelengths (2.5 - 3.5 μm). For example, Figure 2.6 shows carbonaceous chondrite CM Mighei has a small $\sim$0.7 μm absorption which has no noticeable shift as space weathering is simulated, but there is an obvious shift to a higher wavelength for the $\sim$2.7 μm

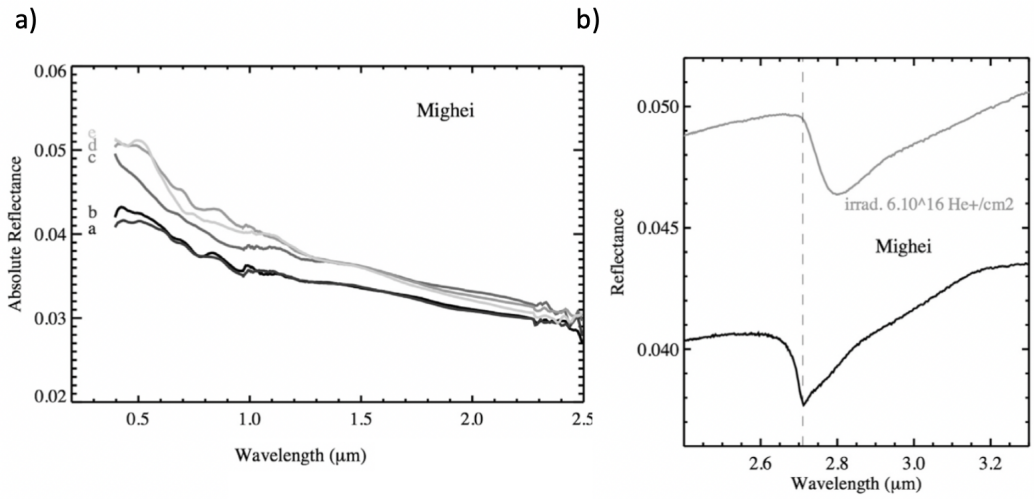

Figure 2.5: (a) CM Mighei carbonaceous chondrite has a small $\sim$0.7 μm absorption band which does not shift much after simulated space weathering. (b) The same sample has a very deep absorption band $\sim$2.7 μm that shifts noticeably toward a longer wavelength after space weathering simulations. (Reprinted from Lantz et al. (2017), with permission from Elsevier.)

absorption for the same carbonaceous chondrite (Lantz et al. 2017).

The 3 μm region presents difficulties for Earth-based observations. The high thermal background and absorption due to water in the Earth's atmosphere make it a challenging observational region (Campins et al. 2018). Specialized telescopes have been able to capture spectra in this region, for example, from the Infrared Space Observatory (ISO) (eg., Barucci et al. 2002). Space telescopes, such as the *Spitzer* Space Telescope, do not have atmospheric interference and have obtained a number of asteroid emissivity spectra (eg., Landsman et al. 2018; Lim et al. 2005). Analyzing where absorption bands and peaks lie on primitive asteroids can guide a simulated space weathering experiment. If the position of the bands in a carbonaceous chondrite spectrum after the experiment do not line up with the position of the bands on primitive asteroids of same mineralogy, the experiment may not be simulating space weathering effects accurately. Primitive asteroid absorption bands can be a constraint on space weathering simulations on carbonaceous chondrites.

Absorption bands in the mid-infrared (MIR; 5 - 16 μm) offer further insight into space

weathering alterations. Space missions, such as NASA's OSIRIS-REx mission to asteroid Bennu, which utilize emission measurements in the MIR can further define absorption band shift on primitive asteroids (Christensen et al. 2018). Future space weathering experiments on carbonaceous chondrites can utilize this data to further validate the accuracy of their simulation.

2.2 Space weathering on C-complex asteroids

Spectroscopic observations of C-complex asteroids show inconsistencies on spectral slope alteration in the VIS-NIR range from space weathering. Lazzarin et al. (2006) used a statistical observation of main belt asteroids using collisional age estimates as a function of asteroid size (Bottke et al. 2005) and combining these with the orbital configuration to obtain a parameter proportional to the exposure to ion flux from the sun. Spectral slopes between 0.52-0.92 μm were used to characterize the degree of space weathering. Lazzarin et al. (2006) concluded a reddening trend for space weathering in C and X-complex asteroids that agreed with S-complex asteroids.

Fornasier et al. (2016) conducted a spectroscopic survey of the Themis and Beagle asteroid families using the 3.56 m Italian Telescopio Nazionale Galileo (TNG) to collect visible and near-infrared spectra. The objects were found to be carbonaceous asteroids with varying spectral slopes and albedo. Themis is an old family (2.5 $\pm$ 1.0 Gyr) (Brož et al. 2013) compared to Beagle ($<$ 10 Myr) (Nesvorny et al. 2008). Objects from the Beagle family are bluer (reflectance decreases with increases wavelength) and higher albedo than the older Themis members, suggesting space weathering may be reddening and darkening these asteroids as well.

Kaluna et al. (2016) performed a similar spectral observation of Themis and Beagle families using the 8.2 m Subaru telescope on Maunakea, Hawaii across the spectral range 0.47-0.91 μm and found 90% of the younger Beagle asteroids to be blue-sloped, while 60% of Themis are blue-sloped. Beagle asteroids were also found to have a higher albedo (0.0794 $\pm$ 0.0045) than Themis (0.0680 $\pm$ 0.0006) asteroids (Kaluna et al. 2016). These results again agree with the C-complex asteroids getting redder and darker due to space weathering.

Other observational studies of C-complex asteroids show a disagreement with the redder/darker S-complex space weathering trends. Nesvorny et al. (2005) used spectra from the Sloan Digital Sky Survey to study color variations between young and old asteroids and found C-complex families to get bluer with age, the opposite of S-complex families. Lantz et al. (2013) compared 43 primitive asteroid spectra with 44 meteorites derived from low-albedo asteroids (CM meteorites). They find Ch/Cgh asteroids to have a bluing effect when compared with the CM meteorites. This is again opposite S-complex families.

Asteroid families with different ages would be expected to show spectral differences due to the amount of space weathering the older objects experience compared to younger objects. An impact event with a parent body would expose unweathered material to space, which would then become space weathered over time (Campins et al. 2018). The Clarissa and Polana families both have similar spectral types (B, C, and X) as well as a lack of a 0.7 micrometer hydration feature (Pinilla-Alonso, 2017; Morate et al. 2018). These similarities lead to Clarissa being known as Polana-like. The Clarissa family is younger (less than 100 million years) than the Polana family (about 2000 million years) (Nesvorny et al. 2015) and there are significant spectral differences between the two families. Figure 2.6 shows the distribution of spectral types in the Polana and Clarissa families (Campins et al. 2018). The older Polana family has a larger fraction of the bluer B-type and a lower fraction of the redder X-type. This trend suggests the lower albedo primitive material is getting bluer the longer it experiences space weathering exposure. This agrees with the Lantz et al. (2015 and 2017) laboratory space weathering simulations.

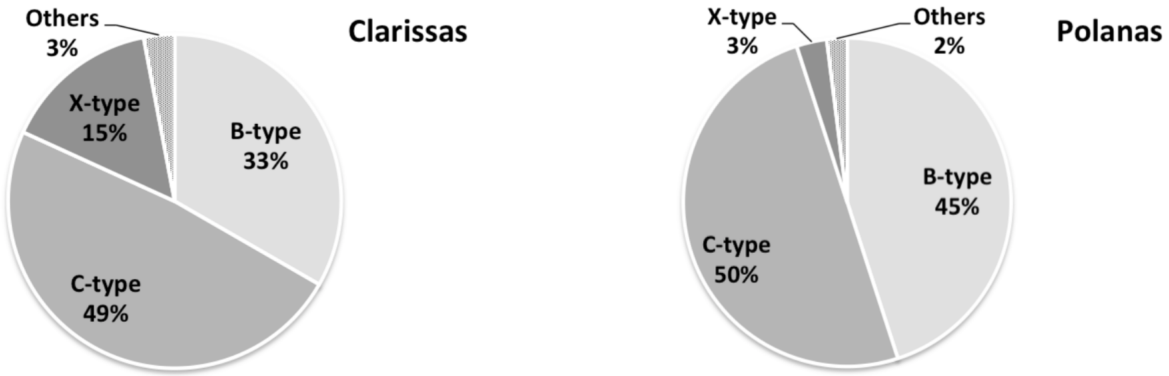

Figure 2.6: Taxonomical groups in the Clarissa and Polana families. The younger Clarissa has a smaller fraction of the bluer B-types and a larger fraction of the redder X-types, suggesting space weathering is causing asteroids to get bluer with age. (Reprinted from Campins et al. (2018), with permission from Elsevier.)

CHAPTER 3: LABORATORY SIMULATIONS

The disagreement in trends for C-complex asteroids experiencing space weathering based on spectroscopic observations has led to an increase in laboratory simulations of space weathering. Laboratory experiments have used several techniques to simulate the effects of space weathering. Solar wind bombardment is simulated through ion irradiation, micrometeorite impacts are simulated through laser irradiation, and impact vaporization is simulated through evaporation and condensation.

3.1 Timescales for space weathering simulations

During space weathering simulations, energy levels must be chosen to accurately recreate timescales asteroids experience space weathering. For solar wind irradiation, ion energy and fluence must simulate the energy of solar wind particles hitting an asteroid a certain distance from the sun over the asteroid's lifespan. For micrometeorite bombardment, laser energy needs to simulate the average impact velocity depending on the asteroid's location.

To estimate a timescale for ion-irradiated Allende, Brunetto et al. (2014) made estimates for four components of ions emitted from the Sun (slow and fast solar wind, events in active regions, and solar flares). They consider an object at 3 AU and an average velocity of 4000 km/s for slow and fast solar wind with a flux of $1.5 \times 10^7 \mathrm{cm}^{-1}\mathrm{s}^{-1}$ (Schwenn et al. 2001). Using an experimental fluence of 3×10^6 He cm^{-2}, an irradiation timescale of $\sim 2 \times 10^3$ years is calculated. Taking into account the energy of the ions used in their experiment, 40 keV, which is about 10 times larger than the average energy of solar wind ions, a more accurate timescale was calculated as $\sim 7 \times 10^3$ years. Taking into account active regions and solar flares, which have known energy spectra (Johnson et al. 1990), an upper limit timescale is calculated ($\sim 2 \times 10^4$ years and $\sim 2 \times 10^5$ years respectively). An approximate corresponding timescale for an ion-irradiation simulation with an energy level of

40 keV and a fluence of 3×10^{16} He cm^2 is $10^3 - 10^4$ years. This process can be repeated for different energies, fluences, and estimations for a corresponding asteroid distance.

The size and velocity of the material colliding with an asteroid surface directly influence the products of micrometeorite bombardment space weathering. The energy level of a pulsed laser determines the type of bombardment being simulated. Dust particles ($\sim$1 μm diameter) with velocities up to 78 km/s will result in ion formation, while larger particles ($\geq$ 10 μm) will lead to the formation of hot plasma (Kissel & Krueger, 1987). To simulate a 1 μm particle impacting at 15 km/s, laser irradiation will need a flux of the order of $10^8 - 10^9$ W/cm^2 and an energy density around $10^{-3} - 1$ J/cm^2 (Kissel & Krueger, 1987). The laser irradiation experiments discussed later have energy densities of the order $10^{-2}\mathrm{J}/\mathrm{cm}^2$.

3.2 Lantz et al. (2017)

Laboratory experiments were performed on carbonaceous chondrites to simulate the effects of solar wind on primitive asteroids. Their samples were crushed into a powder using an agate mortar and pestle resulting in a grain size distribution of 1-100 μm. There was no constraint in the grain size, so the powder created had a wide distribution of grains (Lantz et al. 2017). The powder was then pressed with 7 tons for 10 minutes into a pellet of $\sim$ 100 mg and a diameter of 13 mm on a potassium bromide (KBr) substrate. The KBr substrate is used only to support the pellet and avoid a break. The thickness of the pellet formed ($\sim$ 200 μm) is larger than the penetration depth of both helium (300 $\pm$ 80 nm) and argon (40 $\pm$ 15 nm) found on a simulated Allende-type target (Brunettto et al. 2014), therefore, the ions did not penetrate through the entire pellet. The samples were held vertically on the KBr substrate while irradiated with helium ions from an IRMA ion implanter with an energy of 40 keV and four different, increasing fluences. They used additive doses to get to each total fluence, irradiating the entire surface at each step. The first dose is 5×10^{15} ions/cm^2 and each subsequent step is a multiple of this first dose, resulting in four

fluences of 5×10^{15}, 1×10^{16}, 3×10^{16}, and 6×10^{16} ions/cm^2. Reflectance measurements were made using the INGMAR (IrradiatioN de Glaces et Météorites Analysées par Réflectance VIS-IR, IAS-CSNSM/Orsay) setup, which allows for spectra to be taken from the same position (with an error of less than 100 μm) on the pellet for each fluence dose. Between irradiations and measurements, only the sample holder was moved from the INGMAR chamber to the IRMA ion beamline, while the sample itself remained installed and unmoved. Using the INGMAR setup, bidirectional reflectance spectroscopy in the visible (0.4-1.05 μm) and near-infrared (0.9-2.5 μm) ranges was performed. The collecting spot was 3-4 mm. For the visible range, spectra were collected at Orsay through VIS-NIR fibers coupled to a grating spectrometer Maya2000Pro (Ocean Optics) in the visible range, with a fixed collection angle e = 15°, illumination angle i = 15°, and phase angle 20° because of 3D-geometry. The spectral resolution in the visible was 0.5 nm. In the near-infrared, a Fourier Transform spectrometer Tensor37 (Bruker) was used at ambient temperature, with i = 20°, e = 15°, and a phase angle of 15°. The spectral resolution in the near-infrared was 16 cm^{-1}.

This experimental setup was used on five carbonaceous chondrites, one ungrouped meteorite, and two silicate samples to determine if different meteorite classes will respond differently to the same simulation of space weathering. The silicate sample, olivine, was used to compare to a similar experiment which used an olivine sample (Brunetto et al. 2006). The second silicate sample, diopside, was an easily available sample used to test the experimental setup (Lantz et al. 2017). Both silicate samples had a strong absorption band near 1 μm and their albedo lowered after irradiation, mainly in the VIS range. Brunetto et al. (2006) used argon ions, a higher energy (200 keV), and a lower fluence (7×10^{15} ions/cm^2). The initial spectral curve looks similar to Lantz et al. (2017), with a strong absorption band near 1 μm, and after irradiation, the reflectance lowers most noticeably in the VIS range. Figure 3.1 shows the spectral curves in the VNIR for olivine from Lantz et al. (2017) and Brunetto et al. (2006), as well as a diopside sample from Lantz et al. (2017). The samples of interest are the carbonaceous chondrites, which were CV3 Allende, CO3

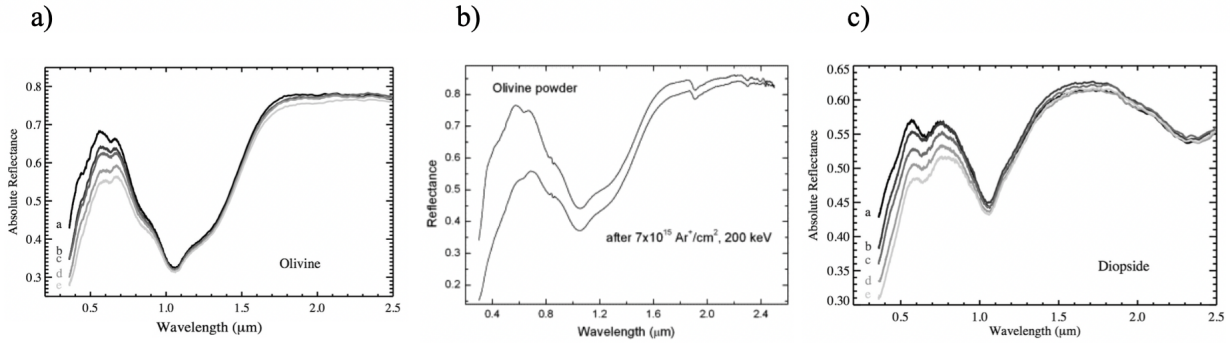

Figure 3.1: (a) Spectral slope in the VNIR of an olivine sample as it experiences irradiation from helium ions (a curve is no irradiation, e curve is highest fluence of 6×10^{16} ions/cm^2) (Reprinted from Lantz et al. (2017), with permission from Elsevier.) (b) Spectral slope in the VNIR of an olivine sample before (top curve) and after (bottom curve) irradiation with argon ions at a fluence of 7×10^{15} ions/cm^2 (Reprinted from Brunetto et al. (2006), with permission from Elsevier.) (c) The same experimental setup as Figure 3.1a, but with a diopside sample. (Reprinted from Lantz et al. (2017), with permission from Elsevier.)

Frontier Mountain, CO3 Lancé, CM2 Mighei, and CI1 Alais.

In the VNIR, the CV3 Allende, CO3 Frontier Mountain, and CO3 Lancé have a similar initial spectra shape. Bidirectional diffuse reflectance spectra show a maximum of reflectance at around 0.6 μm for all three and a strong UV drop-off. With increasing irradiation, the absolute reflectance decreases for all three. Absolute reflectance at 0.55 μm (at 20° phase angle) before any irradiation was 0.173 for CO3 Frontier Mountain, 0.145 for CO3 Lancé, and 0.121 for CV3 Allende (Lantz et al. 2017). After the highest dose of irradiation, the absolute reflectance at 0.55 μm for CO3 Frontier Mountain was 0.147 (2.6% decrease), 0.119 (2.6% decrease) for CO3 Lancé, and 0.103 (1.8% decrease) for CV3 Allende (Lantz et al. 2017). Slopes were evaluated with a linear fit on the range 0.55-2.45 μm for the VNIR and 0.55-1.05 μm for the VIS. Before irradiation and after the highest irradiation dose, CO3 Frontier Mountain VIS-NIR slope increased from -0.204 μm^{-1} to -0.128 μm^{-1}, CO3 Lancé VNIR slope increased from -0.245 μm^{-1} to -0.137 μm^{-1}, and CV3 Allende VNIR slope increased from -0.201 μm^{-1} to -0.124 μm^{-1} (Lantz et al. 2017). There

was an increased slope in the VIS range as well before irradiation and after the highest dose, with CO3 Frontier Mountain going from -0.307 $\mu\mathrm{m}^{-1}$ to -0.026 $\mu\mathrm{m}^{-1}$, CO3 Lancé going from -0.364 $\mu\mathrm{m}^{-1}$ to -0.037 $\mu\mathrm{m}^{-1}$, and CV3 Allende going from -0.333 $\mu\mathrm{m}^{-1}$ to -0.021 $\mu\mathrm{m}^{-1}$ (Lantz et al. 2017). The CV and CO carbonaceous chondrites became darker and the VIS-NIR and VIS slopes increased (reddening of spectra) (Lantz et al. 2017). These results are summarized in Table, from Lantz et al. (2017).

Table 3.1: VNIR spectral parameters before and after helium ion irradiation of 6×10^{16} ions/cm^2. R_0 is the absolute reflectance at 0.55 μm. Slopes were calculated with a linear fit on the whole range (0.55 - 2.45 μm for VNIR, and 0.55 - 1.05 μm for VIS). (Reprinted from Lantz et al. (2017), with permission from Elsevier.)

Sample	R_0		VISNIR slope		VIS slope	
	Before	After irrad.	Before	After irrad.	Before	After irrad.
FM 95002	0.173	0.147	−0.204	−0.128	−0.307	−0.026
Lancé	0.145	0.119	−0.245	−0.137	−0.364	0.037
Allende	0.121	0.103	−0.201	−0.124	−0.333	−0.021
Mighei	0.042	0.050	−0.155	−0.191	−0.322	−0.361
Alais	0.041	0.051	−0.152	−0.149	−0.328	−0.275
Tagish Lake	0.021	0.029	−0.009	−0.130	−0.095	−0.242

Relative to the CV and CO carbonaceous chondrites, CM2 Mighei and CI1 Alais have a lower initial albedo. The maximum absolute reflectance, at about 5 μm, is around 0.04, for the CM2 and the CI1, compared to the CV and COs had maximum absolute reflectance between 0.12 and 0.17 (Lantz et al. 2017). These two chondrites have a similar spectral shape, with an initial peak followed by a gradual decrease in absolute reflectance. Absolute reflectance at 0.55 μm (at 20° phase angle) increased before irradiation and after the highest irradiation dose, from 0.042 to 0.050 (0.8% increase) for CM2 Mighei, and from 0.041 to 0.051 (1% increase) for CI1 Alais (Lantz et al. 2017). The VIS-NIR slope, also evaluated as a linear fit on the range 0.55-2.45 μm, is shown before irradiation and after the highest dose. For CM2 Mighei, slope changed from -0.155 $\mu\mathrm{m}^{-1}$ to -0.191 $\mu\mathrm{m}^{-1}$, and for CI1 Alais, slope changed from -0.152 $\mu\mathrm{m}^{-1}$ to -0.149 $\mu\mathrm{m}^{-1}$ (Lantz

et al. 2017). VIS slope was evaluated on the range 0.55-1.05 μm. Before irradiation and after the highest irradiation dose, the VIS slope for CM2 Mighei changed from -0.322 μm to -0.361 μm, and for CI1 Alais, the VIS slope changed from -0.328 μm to -0.275 μm (Lantz et al. 2017). Absolute reflectance increased for the CM and CI and slope decreased for the CM (became bluer) in the VIS-NIR, however, slope slightly increased for the CI but not outside of the $\sim$0.01 $\mu\mathrm{m}^{-1}$ error for slope evaluation (Lantz et al. 2017).

In order to better visualize how slope changed after each irradiation dose, Lantz et al. (2017) looked at the ratio of altered spectrum divided by unaltered spectrum. They argue since the irradiation experiments are the same for each sample, the effect of the initial composition can be separated from other effects, such as sample preparations, experimental setups, and viewing geometries. The altered spectrum at each dose level is divided by the unaltered spectrum and then the reflectance at 0.55 μm or the slope from linear fit over the range 0.55-2.45 μm is calculated (Lantz et al. 2017). This allows for a clearer visual of how reflectance and slope changes after each dose. Figure 3.2 shows these ratioed reflectance and slope values for each sample at each does level. The color of the dots represent the irradiation dose used in the ratio, green for 5×10^{15} ions/cm^2, blue for 1×10^{16} ions/cm^2, orange for 3×10^{16} ions/cm^2, and red for 6×10^{16} ions/cm^2. For the reflectance values (left graph), the sample is considered to be brightening if the ratio value is greater than one and darkening if the value is less than one. For the VIS-NIR slope (right graph), the sample is reddening if the ratio value is positive and blueing if the value is negative. These graphs show CI1 Alais and CM2 Mighei getting brighter and bluer, while CV3 Allende, CO3 Lancé, and CO3 Frontier Mountain becoming darker and redder (Lantz et al. 2017).

Near to Mid-Infrared (NIR-MIR, 2-16 μm) spectra were also collected using a microanalysis at SMIS (Spectroscopy and Microscopy in the Infrared using Synchrotron) beamline of the Synchrotron SOLEIL (France). Measurements were taken at ambient temperature using a Nicolet iN10 (Thermo Scientific) microscope using the internal Globar light source with a focused beam of 200 μm (confocal reflection) (Lantz et al. 2017). Reference spectra were collected on a gold

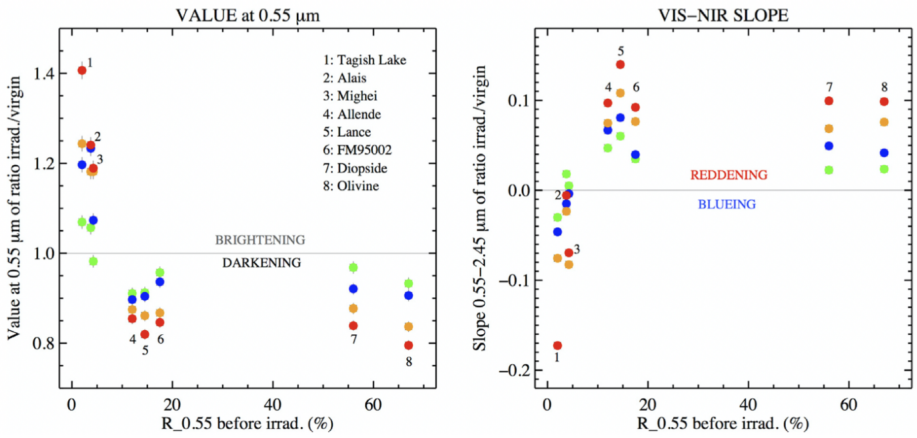

Figure 3.2: The left graph shows a ratio of the reflectance at 0.55 μm before irradiation over irradiated sample for increasing fluence. The right graph shows a ratio of the spectral slope before irradiation over after irradiation of a linear fit over the whole range 0.55 – 2.45 μm. The colors correspond to the same fluences. (Reprinted from Lantz et al. (2017), with permission from Elsevier.)

sample with spectral resolution of 4 cm^{-1}. Measurements were made on spots 200×200 $\mu\mathrm{m}^2$ every 100 μm, covering a grid. Ten or more of these measurements were averaged together to produce spectra (Lantz et al. 2017). These measurements were done on each sample before any irradiation was performed and after the final dose of 6×10^{16} ions/cm^2 (Lantz et al. 2017). This was done to reduce manipulations of the sample being transported to SOLEIL in France. Each spot size was analyzed individually to estimate a position for band peaks at 2.7 and 0.01 μm, with an error of 0.02 μm. The spectral resolution at the 2.7 μm band peak was about 0.001 μm and for the 10 μm band peak, the spectral resolution was about 0.01 μm (Lantz et al. 2017).

Irradiation effects on the samples near the 3 μm feature were characterized by a shift in spectral bands. CM2 Mighei and CI1 Alais both initially had a sharp absorption band at 2.71 $\pm$ 0.01 μm, which shifted to 2.80 $\pm$ 0.01 μm for the CM and 2.78 $\pm$ 0.01 μm for the CI (Lantz et al. 2017).

3.3 Thompson et al. (2019)

Thompson et al. (2019) performed pulsed-laser irradiation on a carbonaceous chondrite meteorite to simulate space weathering effects from micrometeorite bombardment on primitive asteroids. They used a CM2 Murchison meteorite prepared as an unpolished, dry-cut chip, which, they argue, preserves the microscopic properties of the sample better than a powder preparation. Irradiation was conducted with an optically-rastered Nd-YAG, 1064 nm laser with a 1 mm incident beam diameter, using 6-8 ns pulses with an average energy of 48 mJ per pulse (Thompson et al. 2019). A raster pattern over an area $\sim$0.5 cm^2 was used to minimize overlap while exposing an irradiated area to a similar laser fluence. The experimental setup also involved a silica glass slide collection substrate ($\sim$7 mm away from the sample) in which a vapor plume produced from the laser interacting with the sample condenses on the surface (Thompson et al. 2019). The laser first passed through the glass slide before interacting with the sample. The condensed deposit was then analyzed for its spectral properties and chemical characteristics.

Reflectance spectroscopy in the 0.35-2.5 μm range was measured under ambient laboratory conditions with a fiber-optic ASD FieldSpec 3 Spectrometer from Malvern Panalytical at the Johnson Space Center. The spectral resolution used was 0.003 μm at 0.7 μm, 0.0085 μm at 1.4 μm, and 0.0065 μm at 2.1 μm (Thompson et al. 2019). This spectrometer used a MugLite probe for spectral measurements of unirradiated and irradiated samples, which has an incandescent light source in a parabolic reflector held at a 55° angle from the viewing plane, while the fiber was held at a 78° angle from the viewing plane (Thompson et al. 2019). Reflectance was calibrated against a Spectralon white standard (Labsphere SRS-99-010), which was also used to place the silica glass slide on top off in order to take spectral measurements of the deposited material. Environment for Visualizing Images (ENVI) software by Harris Geospatial Solutions was used for continuum removed spectra (Thompson et al. 2019).

To analyze the chemical composition and morphology of the laser-irradiated surface and

the collected vapor deposit, a JEOL 7600F field-emission scanning electron microscope (SEM) was used at the Johnson Space Center (Thompson et al. 2019). The SEM had a Thermo silicon drift energy dispersive X-ray (EDX) spectrometer equipped. Four electron-transparent thin sections ($\sim$100 nm) from areas of the sample chosen from SEM images and extracted using a focused ion beam (FIB) from an FEI Quanta 3D FIB (Thompson et al. 2019). These sections were analyzed with a JEOL 2500SE 200 kV field-emission scanning transmission electron microscope (STEM), using a thin-window Thermo EDX 50 mm^2 detector. SEM observations of the irradiated CM2 sample showed a "frothy surface texture" (Thompson et al. 2019) in the fine-grained matrix with indications of burst vesicles. Another section of the meteorite, an Fe-Ni-sulfide grain, had a similar texture to the matrix material with sub-micrometer pitting, also suggestive of burst vesicles (Thompson et al. 2019). An olivine grain on the irradiated meteorite does not have these features (vesiculation, pitting, "frothy" texture) but does have indications of melting (Thompson et al. 2019).

SEM images of the vapor deposit on the glass slide show circular $\sim$15 mm deposits uniformly dispersed, representing material deposited from individual laser pulses (Thompson et al. 2019). Higher magnification of these deposits show oblong and circular deposits up to several hundred nanometers thick. EDX maps of these deposits showed a composition of Mg (18 at.%), Si (22 at.%), and Ca (localized regions of up to 5 at.%) (Thompson et al. 2019). Selected area electron diffraction (SAED) of the nanoparticles in the deposits showed at least three individual phases, including troilite, pentlandite, and magnetite (Thompson et al. 2019). The spectral slope of the deposited material over the VIS-NIR (0.35-2.5 μm) is red-sloped compared to the spectra on the unirradiated sample over the same range, which Thompson et al. (2019) infer to be a result of the disseminated sulfide nanoparticles, troilite and pentlandite. Slope values are not calculated but the slope of the irradiated spectra is very clearly steeper than the unirradiated spectra, seen in Figure 3.3 (Thompson et al. 2019).

The reflectance spectra of the irradiated surface shows darkening over the entire VIS-NIR

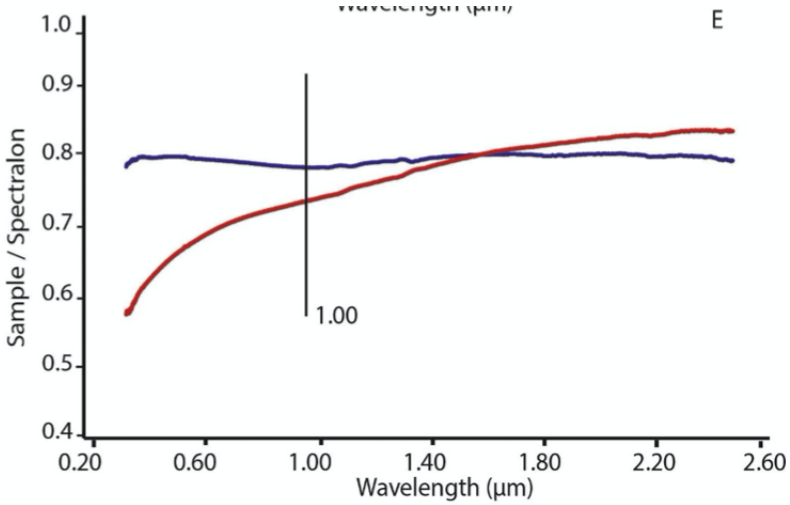

Figure 3.3: Spectra from the deposit collected on the glass slide (red line) compared with spectra of the unirradiated surface (blue line). (From Thompson et al. (2019).)

wavelength (Thompson et al. 2019). This could be contributed to the change in roughness after irradiation from relatively smooth, dry-cut surface to a rougher, diffuse surface (Thompson et al. 2019). Spectral surface darkening and a reddened slope for the collected vapor deposits for this CM sample is the opposite reaction of what Lantz et al. (2017) concluded for their CM sample.

3.4 Nakamura et al. (2019)

Using the same experimental setup as Lantz et al. (2017), ion irradiation on carbonaceous chondrites CM MET01072 and CI Y 980115. They used 20 keV He irradiation at CSNSM-IAS Orsay, France, at dose levels of 1×10^{16}, 3×10^{16}, and 6×10^{16} ions/cm^2 (Nakamura et al. 2019). Both samples were prepared as a 1 cm sized, flat surface chip with roughness made by a #400 polishing disk (Nakamura et al. 2019). The CI sample was also prepared as a powder with 155 μm grain size and then pressed into a pellet with the same method used in Lantz et al. (2017). Reflectance spectra were taken of the same portion of each sample before and after irradiation in the wavelength range 0.45-11.5 μm in France and then double checked in Japan in the 0.4-

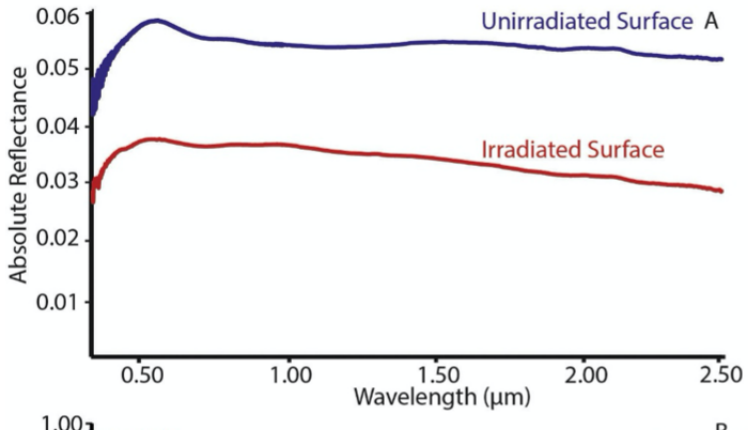

Figure 3.4: Reflectance spectra of the unirradiated surface (blue line) and the irradiated surface (red line). (From Thompson et al. (2019).)

15 μm range for the unirradiated samples and after the highest dose (Nakamura et al. 2019). Specifics of how reflectance was measured or calculations for slope values are not provided, as this is experiment is currently in abstract form. There is also no spectra or figures.

For the CM sample (chip preparation), had mostly flat, featureless spectra in the range 0.4-1.0 μm (Nakamura et al. 2019). With increasing ion irradiation dose, the sample became spectrally brighter and the slope became bluer (Nakamura et al. 2019). When the CI sample was prepared as either a chip or a pellet, it showed nearly featureless spectra in the range 0.4-1.0 μm and 6-7% reflectance at 0.55 μm (Nakamura et al. 2019). Increasing ion irradiation dosage resulted in bluing and brightening for the pellet sample, and reddening with no significant brightening for the chip sample (Nakamura et al. 2019). Spectral changes are dependent on the physical properties (sample preparation) of the carbonaceous chondrites. The chip was described as more porous than the pellet (Nakamura et al. 2019), however, it is unclear if this would have an influence on the difference in spectral changes. Space weathering spectral results are dependent on sample preparation. The same experiment produced different results when the sample was prepared differently.

CHAPTER 4: LABORATORY EXPERIMENT TRENDS

I investigate various laboratory simulations to determine if experimental conditions lead to a pattern in spectral response to simulated space weathering on carbonaceous chondrites. Looking at the experiments by Lantz et al. (2017), Thompson et al. (2019), and Nakamura et al. (2019), it is clear different sample preparation, different types of carbonaceous chondrites, and different simulation methods (laser irradiation or ion irradiation) can all result in different spectral alterations. I examined 33 space weathering simulations to see if there are trends spectral response due to the type of carbonaceous chondrite, sample preparation, or space weathering process being simulated.

To compare the observed spectral differences between space weathering experiments, the spectral results are compared for different experimental variables. Figure 4.1 shows the results as colors (blue or red sloped spectra and albedo darkening or brightening) with the x-axis showing the change in carbonaceous chondrite being weathered and the y-axis showing the number of experiments that fit into each grouping. CVs and CMs are the most commonly tested, with CVs having a clear favor of red/dark spectral change and CMs having much more variety.

Nakamura et al. (2019) showed the importance of sample preparation in space weathering experiments. The two types of sample preparations they investigated were either crushing the meteorite in a powder and pressing the powder into a pellet or cutting a chip from the sample. Figure 4.2 shows a comparison of space weathering simulation results for the two types of sample preparation. There are far fewer experiments on chip samples than powder/pellet samples. The experiment by Nakamura et al. (2019) on a chip of CI carbonaceous chondrite is not shown these graphs because it did not have an albedo change after being weathered. As mentioned earlier, their experiment is important to note because it showed how changing the sample preparation can change the results from space weathering simulations.

Space weathering experiments will either simulate the process through ion irradiation or laser irradiation. This is to simulate the effects of solar wind or micrometeorite bombardment.

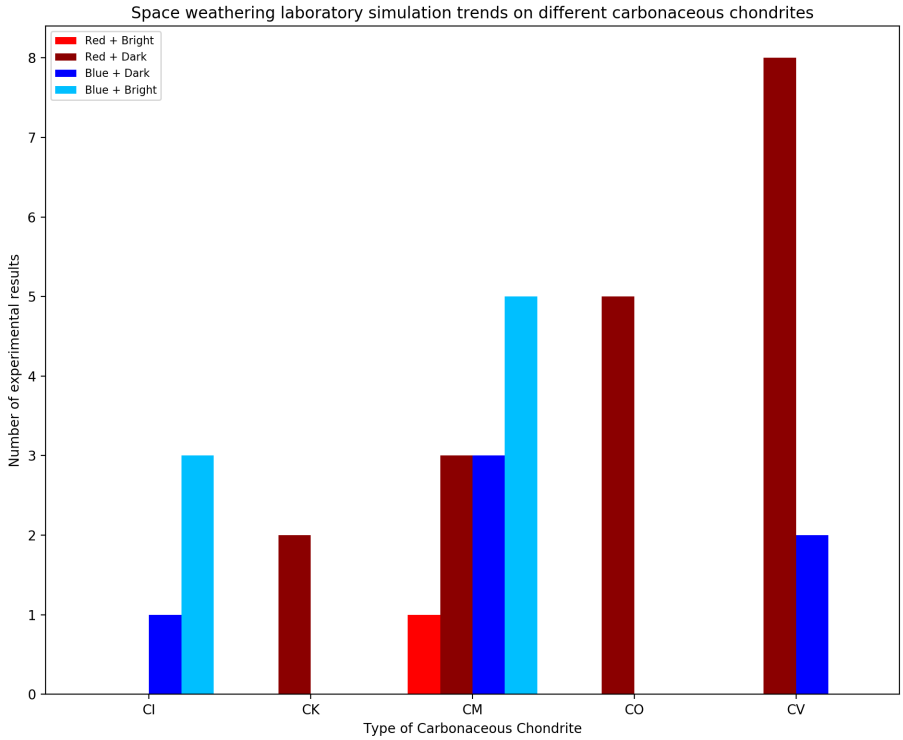

Figure 4.1: Trends for 33 space weathering laboratory experiments on carbonaceous chondrites, separated by meteorite type (x-axis). The light red bar represents the sample becoming redder and brighter, the dark red bar represents the sample getting redder and darker, the light blue bar represents the sample getting bluer and brighter, and the dark blue bar represents the sample getting bluer and darker.

Both are important in the space weathering process but the question of which is more important is dependent on many factors such as distance from the sun, age of the asteroid, and proximity to other bodies such as the asteroid belt. Figure 4.3 shows the spectral trends for laboratory experiments on carbonaceous chondrites separated into the two space weathering simulation processes. Micrometeorite simulations only have red/dark or blue/dark trends and solar wind simulations have only red/dark or blue/bright results except for one red/bright result seen by Lantz et al. (2015b).

The energy levels used in each experiment are shown in Table 4.1. For experiments that

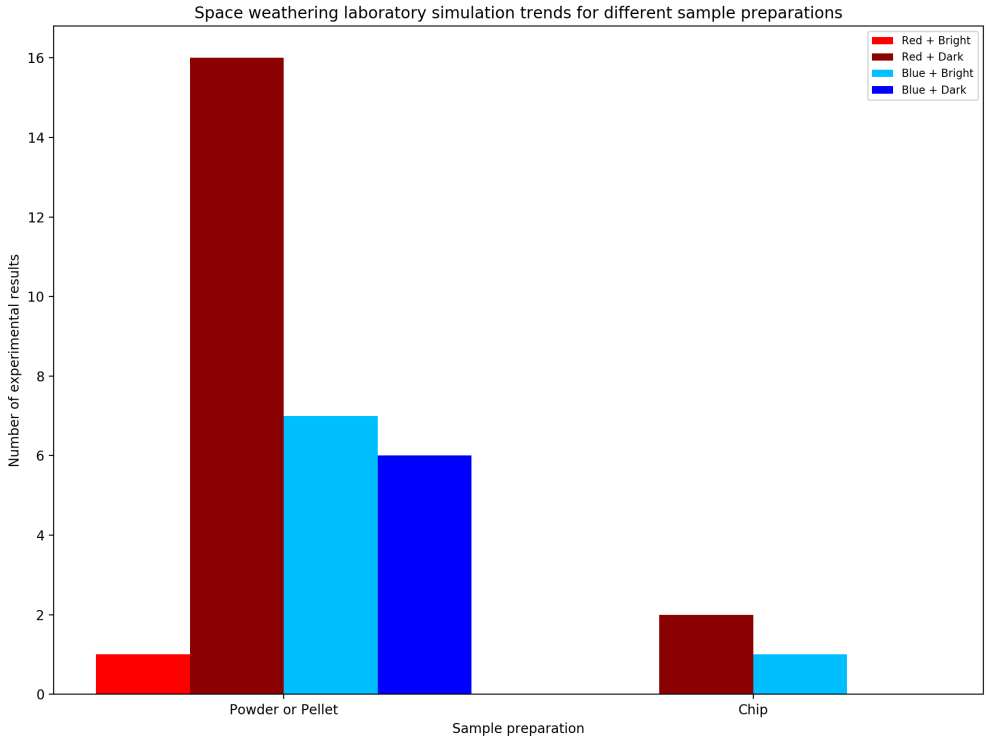

Figure 4.2: Trends for 33 space weathering laboratory experiments on carbonaceous chondrites, separated by sample preparation (x-axis). Their spectral change is shown by the color of the bars.

used ion irradiation to simulate solar wind, the type of ion (helium ions or argon ions) are noted as well as the fluences used. The pulse duration for the experiments that used laser irradiation to simulate micrometeorite bombardments are shown in the last column.

Figure 4.4 combines the three experimental variables to see if there is a trend between their combinations and the spectral results produced. Lantz et al. (2017) predicted carbonaceous chondrites initially relatively bright will become darker while relatively darker ones will become brighter. They separated their studied carbonaceous chondrites into a relatively darker initial albedo (CI/CM) and a relatively brighter initial albedo (CV/CO). Figure 4.4 shows CV/CO chondrites favoring a red/dark trend and CI/CM chondrites favoring a blue/bright trend. There are

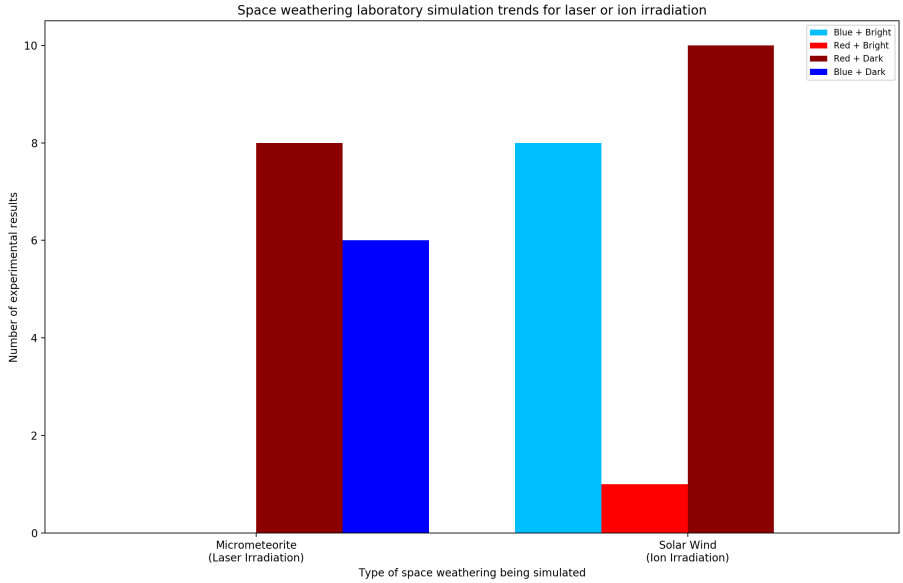

Figure 4.3: Trends for 33 space weathering laboratory simulations separated into the two types of simulations: solar wind (through ion irradiation) and micrometeorite bombardment (through laser irradiation). Their spectral trend is shown by the color of the bars.

disagreements for this type of grouping between experiments. CV/CO has 13 dark/red trends and 2 dark/blue trends. CI/CM has 8 bright/blue trends, 4 dark/blue trends, 3 dark/red trends, and 1 bright/red trend. Lantz et al. (2017) demonstrated the benefit of experimental setup on various chondrite types, while Nakamura et al. (2019) showed a similar benefit by testing two different sample preparations for the same meteorite and simulation type. By comparing 33 experimental results, I show a disagreement in space weathering simulation results depending on sample type and experimental setup. This suggests the experiments may be over simplifying the space weathering process. More accurate space weathering simulations should replicate their experiment with multiple setups and with various carbonaceous chondrite types.

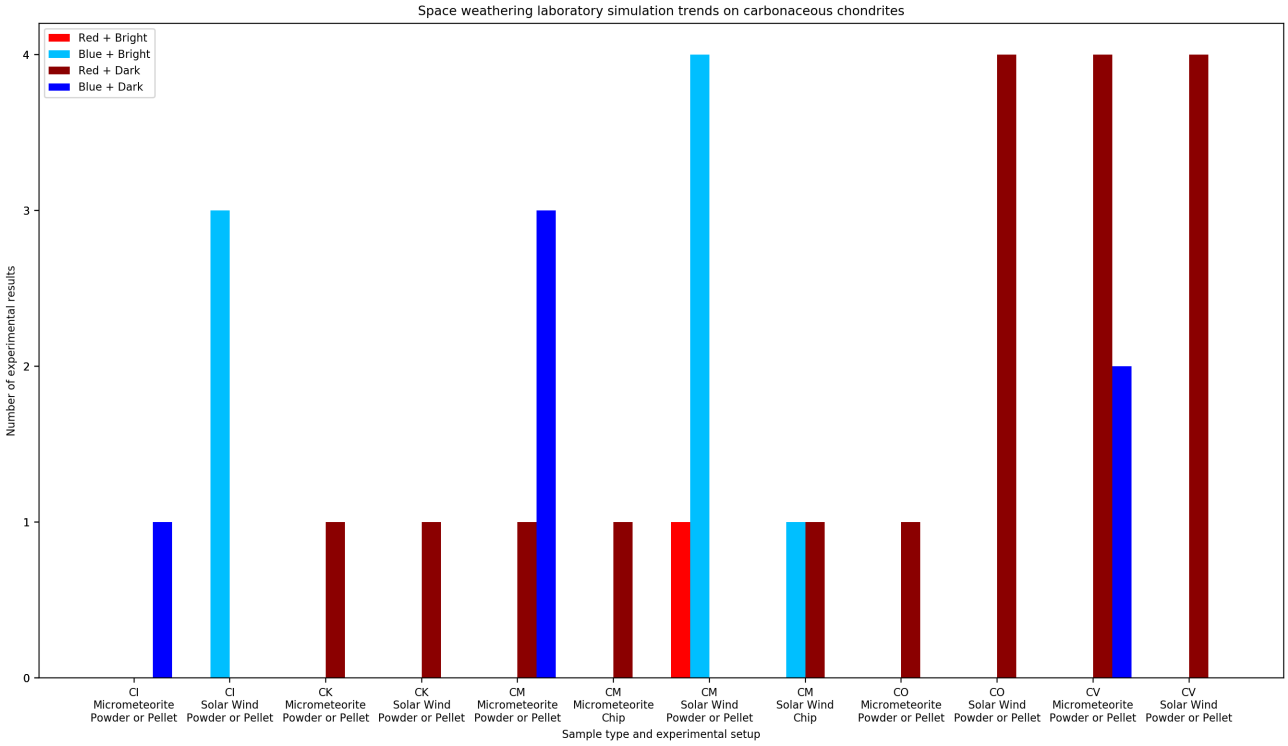

Figure 4.4: Spectral results of 33 laboratory simulations of space weathering on carbonaceous chondrites, separated into each combination of carbonaceous chondrite type, space weathering simulation, and experimental setup. Their spectral change is shown by the color of the bars.

Table 4.1: Energy levels for each experiment. The type of ion used for ion irradiation experiments is shown, as well as the fluences used. The pulse duration is shown for laser irradiation experiments.

Paper	Energy Level	Ion type	Fluences	Pulse Duration
Brunetto et al. 2014	40 keV	He+ and Ar+	He+: 3E+16; Ar+: 6E+15	N/A
Gillis Davis et al. 2013	30mJ	N/A	N/A	5-7 ns for 10 minutes
Gillis Davis et al. 2015	30mJ	N/A	N/A	5-7 ns for 40 minutes
Gillis Davis et al. 2017a	30mJ	N/A	N/A	6-7 ns, 48,000 pulses
Gillis Davis et al. 2017b	30mJ	N/A	N/A	5-7 ns for 40 minutes
Hiroi et al. 2013	5 and 10 mJ	N/A	N/A	6-8 ns
Keller et al. 2015	4 keV	He+	1E+18	N/A
Lantz et al. 2015a	40 keV	He+	6.00E+16	N/A
Lantz et al. 2015b	40 keV	He+ and Ar+	3.00E+16	N/A
Lantz et al. 2017	40 keV	He+	6.00E+16	N/A
Lantz et al. 2019	40 and 15 keV	He+	6.00E+16	N/A
Lazzarin et al. 2006	400 keV	Ar+	9.40E+15	N/A
Matsuoka et al. 2015	5, 10, and 15 mJ	N/A	N/A	6-8 ns
Matsuoka et al. 2016	5 mJ	N/A	N/A	N/A
Moroz et al. 2004	Not specified	N/A	N/A	N/A
Nakamura et al. 2019	20 keV	He+	6.00E+16	N/A
Thompson et al. 2019	48mJ	N/A	N/A	6-8 ns

CHAPTER 5: RYUGU

The Hayabusa2 mission to asteroid 162173 Ryugu, which arrived in June 2018, has allowed for close, thorough observations of a near-Earth carbonaceous asteroid (Sugita et al. 2019), allowing insight into how space weathering alters this type of object. Hayabusa2 made use of the Optical Navigation Camera-Telescopic (ONC-T), with seven narrowband filters, a wideband filter, a Thermal Infrared Imager (TIR) a Near-Infrared Spectrometer (NIRS3) and a laser Light Detection and Ranging system (LIDAR) (Watanabe et al. 2019). Regolith spectra from ONC-T, when compared to main-belt, C-complex asteroids, are consistent with moderately dehydrated CCs, such as CM or CI chondrites (Sugita et al. 2019). Morota et al. (2019) used ONC-T images to identify craters and compare the spectra in the underlying crater to the surrounding surface. 15 craters with a diameter ranging from 10 to 50 m were found to have spectrally a spectrally blue slope compared to the surrounding material (Morata et al. 2019). This suggests the underlying material, which was covered for some time before being excavated, experienced less space weathering than the surrounding material, so the material is becoming more red-sloped with increasing space weathering. Figure 5.1 shows the ONC-T image with the craters pointed out and a b-x slope image (0.48-0.86 μm) (Morata et al. 2019).

Reflectance spectra of Ryugu's surface (1.8 - 3.2 μm) from the NIRS3 reveal a narrow absorption feature centered at 2.7 μm, an indicator of hydroxyl (OH)-bearing minerals (Kitazato et al. 2019). This feature was detected across the entire observed surface of Ryugu. Combined with Ryugu's low geometric albedo ($4.5 \pm 0.2\%$ at 0.55 μm; Sugita et al. (2019)) suggest a carbonaceous chondrite-like body, however the spectra does not exactly match with any carbonaceous chondrite meteorites. Figure 5.2 shows thermally corrected spectrum from the NIRS3 (Kitazato et al. 2019) with the 2.72 μm feature indicated. Figure 5.3 shows a comparison of Ryugu's reflectance spectra with spectra of carbonaceous chondrites which are possible spectral matches (Kitazato et al. 2019). These carbonaceous chondrites are Ivuna (CI1), Cold Bokkeveld (CM2), MET 01072

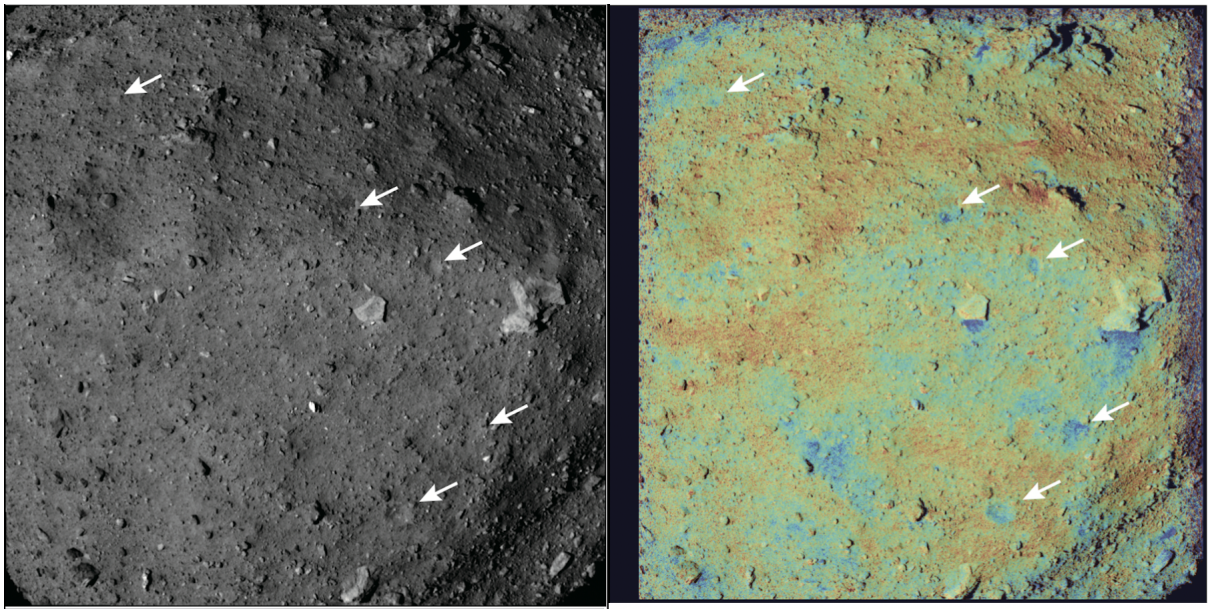

Figure 5.1: Crater locations on Rygu. The second image shows the blue material exposed underneath the red surface. (From Morota et al. (2019), used with permission from Tomokatsu Morota.)

(shocked CM2), and Allende (CV3) (Kitazato et al. 2019).

Because Ryugu is likely a CI, CM, or CV chondrite-like asteroid (Kitazato et al. 2019), looking at the experiments by Lantz et al. (2017) and Thompson et al. (2019) on these types of carbonaceous chondrites may give insight into which experiment is the most accurate space weathering simulation for Ryugu. The spectra from NIRS3 of Ryugu has a wavelength range from 1.8 - 3.2 μm, so looking at these same ranges in Figure 5.4a - 5.4e, the spectral slope should be red (increasing reflectance) until the 2.72 μm absorption band. Space weathering experiments replicated Ryugu should spectral slope becoming more red. CI Alais, CM Mighei, and CV Allende are all blue-sloped in this range, while CM2 Murchison is mostly flat. As mentioned in Section 3.2, CI Alais and CM Mighei became more blue-sloped after irradiation and CV Allende became more red-sloped. In Section 3.3, the spectrum of the glass slide deposit for the CM2 Murchison showed a red-sloped spectra after irradiation. CV Allende and CM2 Murchison both satisfy the

red-sloped space weathering trend. Only CI Alais and CM Mighei has NIR spectral data, and they both have a 2.71 μm absorption band that shifts toward a longer wavelength after irradiation. This seems to agree with the Ryugu spectra, which has an absorption band centered at 2.72 μm, slightly higher than the initial 2.71 μm CI Alais and CM Mighei had. The two samples with NIR data have absorption band shift that agrees with Ryugu spectral data, but the VNIR slope change does not agree. The two samples that have agreeing VNIR slope change do not have NIR data to show a possible absorption band near 2.72 μm.

Ryugu spectral data also shows a very low albedo, much lower than any of the experiments from Lantz et al. (2017) and Thompson et al. (2019). Kitazato et al. (2019) suggests this may be due to a high abundance of carbon, opaque minerals (such as magnetite), and/or shock-induced metamorphism causing dark, glassy components. Space weathering experiments should result in the sample having a lower albedo, which only happens for the CM2 Murchison and CV Allende samples. Based on these observations, CM2 Murchison and CV Allende have the most evidence supporting them as accurate representations of space weathering on Ryugu. For the three experiments in Nakamura et al. (2019), the CI chip sample agreed most with Ryugu spectra, with spectral slope becoming more red and reflectance having no significant change.

A spectral slope map of Ryugu's surface from b-band (0.48 μm) to x-band (0.86 μm) shows a bluer spectral slope at the poles, equatorial ridge, and in large troughs (Figure 5.2; Sugita et al. 2019). Polar regions and equatorial ridge are topographical highs, which Sugita et al. (2019) suggest may be subject to gradual erosion, exposing the fresh surface material. Sugita et al. (2019) also point out locations such as crater floors are likely to have a build-up of deposition. These areas have spectrally redder and darker material, suggesting Ryugu's surface experiences spectral reddening and darkening over time (Sugita et al. 2019). This agrees with the reflectance spectra of Ryugu's surface discussed above. Ryugu has a very low reflectance and the spectral slop in the VNIR is more red than the initial spectral slope of the carbonaceous chondrite samples from Lantz et al. (2017) and Thompson et al. (2019).

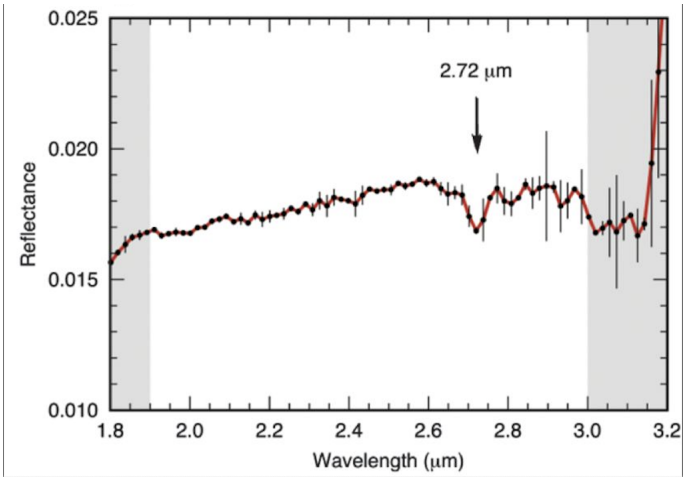

Figure 5.2: Thermally corrected reflectance spectra of the observed surface of Ryugu from the NIRS3, with a 2.72 μm absorption band indicated, which was detected across the entire surface of Ryugu. (From Kitazato et al. (2019). Reprinted with permission from AAAS.)

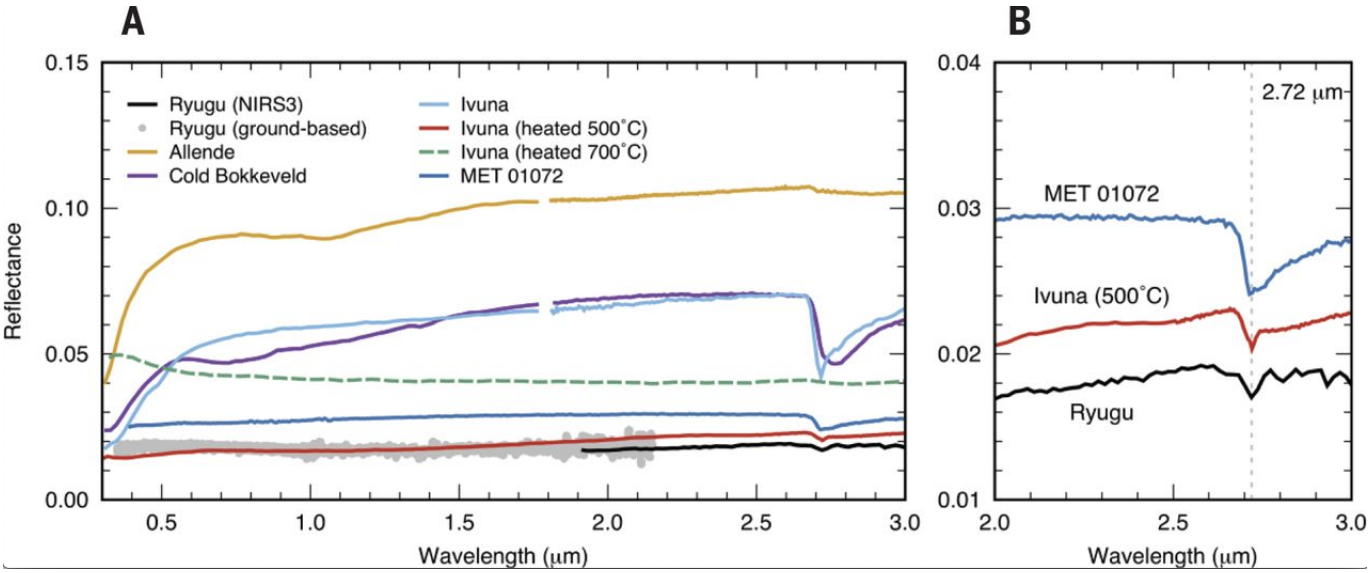

Figure 5.3: Globally averaged reflectance spectra of Ryugu compared with carbonaceous chondrite meteorite samples: Ivuna (CI1), Cold Bokkeveld (CM2), MET 01072 (shocked CM2), and Allende (CV3). (From Kitazato et al. (2019). Reprinted with permission from AAAS.)

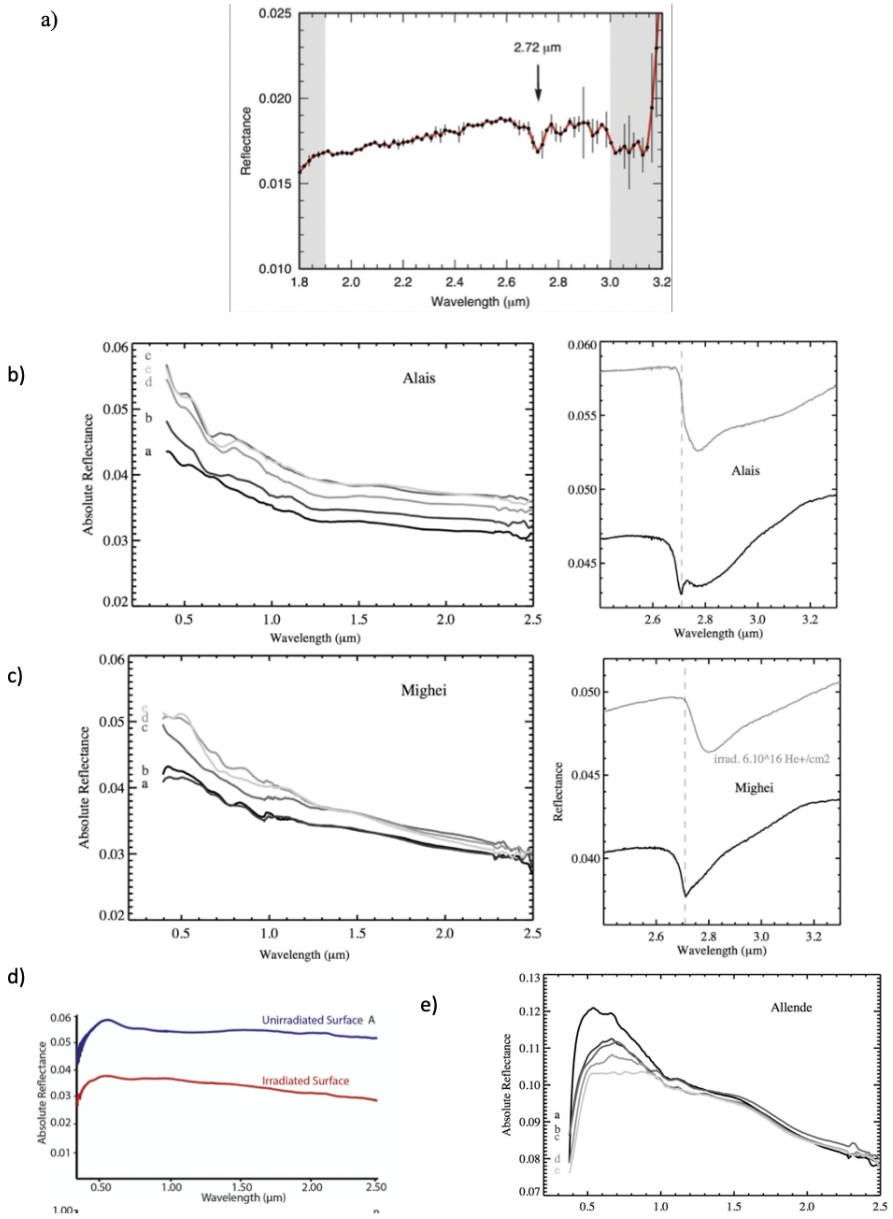

Figure 5.4: (a) (Same as Figure 5.2) Reflectance spectra of Ryugu from the NIRS3. (From Kitazato et al. (2019). Reprinted with permission from AAAS.) (b) Spectra of CI Alais in the VNIR and NIR before and after irradiation. (Reprinted from Lantz et al. (2017), with permission from Elsevier.) (c) Spectra of CM Mighei in the VNIR and NIR before and after irradiation. (Reprinted from Lantz et al. (2017), with permission from Elsevier.) (d) Spectra of CM2 Murchison in the VNIR before and after irradiation. (From Thompson et al. (2019).) (e) Spectra of CV Allende in the VNIR before and after irradiation. (Reprinted from Lantz et al. (2017), with permission from Elsevier.)

Ryugu is classified as a rubble-pile asteroid, with large porosity and large ($>$ 1 cm) grains across its surface (Watanabe et al. 2019). Laboratory space weathering experiments would want to recreate this type of surface to have more accurate initial conditions. A chip sample reflects a rubble-pile asteroid more closely than a crushed powder, however, the high porosity of Ryugu suggests a powder sample would actually be more accurate. The low thermal inertia of large boulders on Ryugu suggest they are very porous (Sugita et al. 2019). Lantz et al. (2017) powder preparation created a grain size distribution of 1-100 μm, much smaller than the large grains of Ryugu. Lantz et al. (2017) has mid-infrared (0.4 - 16 μm) spectra for six of the powdered samples they used. They all have a strong 10 μm emissivity band, an indicator of high porosity (Vernazza et al. 2012). Lantz et al. (2017) results for CI and CM carbonaceous chondrites became spectrally bluer with increasing irradiation, the opposite of how Ryugu appears to be weathering. Thompson et al. (2019) has an agreeing spectral trend for their CM sample prepared as a chip. Nakamura et al. (2019) agreed with Ryugu when their CI sample was prepared as a chip, but disagreed when their CI was prepared as a powdered pellet. Although the chip samples seem to agree with observed space weathering on Ryugu, the high porosity of the boulders on Ryugu suggests a powder sample preparation should be a more accurate representation for space weathering simulations.

CHAPTER 6: CONCLUSIONS

Sample return missions, like Hayabusa2 to Ryugu and NASA's OSIRIS-REx mission to asteroid Bennu, provide the best possible resource for understanding space weathering on C-type asteroids and carbonaceous chondrites. Reflectance spectra of Ryuga collected from Hayabusa2 with the NIRS3 shows how the spectral slope of a space weathering simulation should look after the experiment is completed. Understanding the type of surface (rubble-pile, fine grained, etc.) gives an idea of how a sample should be prepared in space weathering simulations. Ryugu is a rubble-pile asteroid, which would imply a chip preparation, however, the large boulders are very porous, which aligns with a powder sample. Returned samples will give the clearest idea of the space weathering process on C-type asteroids. TEM images will be possible to show what minerals or melts are being formed on the regolith and will give a better starting point for simulation experiment design. Emission measurements in the MIR, such as those possible with OSIRIS-REx Thermal Emission Spectrometer (OTES), will provide more information on how absorption bands shift on primitive asteroids (Christensen et al. 2018). Sample returns from Itokawa helped our understanding of space weathering on S-type asteroids and ordinary chondrites. Sample returns from C-type asteroids will help our understanding of space weathering on carbonaceous chondrites.

Space weathering effects on S-type asteroids is well established, however, effects on primitive asteroids is still unclear. Laboratory experiments simulating space weathering on carbonaceous chondrites have revealed the process to be more complex than on ordinary chondrites. Ryugu has a unique physical structure, with a rubble-pile surface that is also very porous. The rocky nature would suggest the chip samples from Thompson et al. (2019) and Nakamura et al. (2019) most closely represent Ryugu, however, the porosity suggests Ryugu more closely resembles a powder preparation as in Lantz et al. (2017). The experiments by Lantz et al. (2017) predict the opposite spectral change than what is observed on Ryugu, showing sample preparation alone is not enough to accurately represent space weathering on Ryugu. The type of simulation (laser irradiation or ion

irradiation) can change the result of the simulation. Laser irradiation causes shock, melting, and vaporization of grains, while ion irradiation causes energy transfers that create chemical reactions in the sample. Experiments focus on one or the other when simulating space weathering on their sample. Recreating an experiment with the same setup and sample preparation but using a different simulation type could show how the reflectance spectra reacts differently.

Thompson et al. (2019) investigated the chemical composition of their sample using a SEM and STEM, however, Lantz et al. (2017) did not. Having these images to compare what was being produced during the simulations could clearly show why the change in spectra differed. SEM images are necessary to understand how changes in an experimental design alters the complex space weathering process for carbonaceous chondrites.

I investigated 33 different laboratory experiments to determine a pattern from three experimental variables. Sample preparation (powder/pellet or chip), type of space weathering being simulated (solar wind or micrometeorite bombardment), and type of carbonaceous chondrite being sampled all influence the spectral changes (red or blue sloped, increased or decreased albedo). The lack of a clear trend suggests the experiments may not be representing the complex space weathering process for primitive asteroids.

As data from Ryugu continues to be analyzed, and samples are eventually returned to Earth, future laboratory space weathering experiments will have more information to assist in creating more accurate representations of space weathering on carbonaceous chondrites. The disagreements between the experiments so far and the demonstration by Nakamura et al. (2019) of experimental setup changing space weathering effects suggest most experiments are over-simplifying their simulated space weathering process. Future experiments should account for multiple space weathering variables in order to better grasp the full process.

REFERENCES

Adams, J. B., & Jones, R. L. (1970). Spectral reflectivity of lunar samples. *Science, 167*(3918), 737-739.

Adams, J. B., & McCord, T. B. (1970). Remote sensing of lunar surface mineralogy: Implications from visible and near-infrared reflectivity of Apollo 11 samples. *Geochimica et Cosmochimica Acta Supplement*, 1, 1937.

Adams, J. B., & McCord, T. B. (1971). Alteration of lunar optical properties: Age and composition effects. *Science, 171*(3971), 567-571.

Adams, J. B., & McCord, T. B. (1971). Optical properties of mineral separates, glass, and anorthositic fragments from Apollo mare samples. In *Lunar and Planetary Science Conference Proceedings* (Vol. 2, p. 2183).

Allen, C. C., Morris, R. V., & McKay, D. S. (1996, March). Experimental approaches to space weathering. In *Lunar and Planetary Science Conference* (Vol. 27).

Baratta, G. A., Fulvio, D., Garozzo, M., Gomis, O., Leto, G., Palumbo, M. E., ... & Strazzulla, G. (2008). Ion implantation in ices of interest for planetology. *Memorie della Societa Astronomica Italiana Supplementi,* 12, 126.

Barucci, M. A., Dotto, E., Brucato, J. R., Müller, T. G., Morris, P., Doressoundiram, A., ... & Le Bras, A. (2002). 10 Hygiea: ISO infrared observations. Icarus, 156(1), 202-210.

Bennett, C. J., Pirim, C., & Orlando, T. M. (2013). Space-weathering of solar system bodies: A laboratory perspective. *Chemical reviews*, 113(12), 9086-9150.

Britt, D. T. (1991). *The meteorite record as clues to asteroidal regolith processes*, Brown University PhD (Doctoral dissertation, thesis).

Brunetto, R., & Strazzulla, G. (2005). Elastic collisions in ion irradiation experiments: A mechanism for space weathering of silicates. *Icarus*, 179(1), 265-273.

Brunetto, R., Vernazza, P., Marchi, S., Birlan, M., Fulchignoni, M., Orofino, V., & Strazzulla, G. (2006). Modeling asteroid surfaces from observations and irradiation experiments: The case of 832 Karin. *Icarus*, 184(2), 327-337.

Brunetto, R. (2009). Space weathering of small solar system bodies. *Earth, Moon, and Planets*, 105(2-4), 249-255.

Brunetto, R., Lantz, C., Ledu, D., Baklouti, D., Barucci, M. A., Beck, P., ... & Engrand, C. (2014). Ion irradiation of Allende meteorite probed by visible, IR, and Raman spectroscopies. *Icarus*, 237, 278-292.

Brunetto, R., Loeffler, M. J., Nesvorný, D., Sasaki, S., & Strazzulla, G. (2015). Asteroid surface alteration by space weathering processes. *Asteroids iv*, 597-616.

Burbine, T. H., McCoy, T. J., Jarosewich, E., & Sunshine, J. M. (2003). Deriving asteroid mineralogies from reflectance spectra: Implications for the MUSES-C target asteroid. *Antarctic meteorite research.*

Burbine, T. H. (2016). Reflectance Spectroscopy and Asteroid Taxonomy. In *Asteroids: Astronomical and Geological Bodies*, Cambridge Planetary Science (pp. 133–184). chapter, Cambridge: Cambridge University Press.

Campins, H., Morbidelli, A., Tsiganis, K., De León, J., Licandro, J., & Lauretta, D. (2010). The origin of asteroid 101955 (1999 RQ36). *The Astrophysical Journal Letters*, 721(1), L53.

Campins, H., de León, J., Licandro, J., Hendrix, A., Sánchez, J. A., & Ali-Lagoa, V. (2018). Compositional diversity among primitive asteroids. In *Primitive Meteorites and Asteroids* (pp. 345-369). Elsevier.

Chapman, C. R., Morrison, D., & Zellner, B. (1975). Surface properties of asteroids: A synthesis of polarimetry, radiometry, and spectrophotometry. *Icarus*, 25(1), 104-130.

Chapman, C. R. (2004). Space weathering of asteroid surfaces. *Annu. Rev. Earth Planet. Sci.*, 32, 539-567.

Christensen, P. R., Hamilton, V. E., Mehall, G. L., Pelham, D., O'Donnell, W., Anwar, S., ... & Fisher, T. (2018). The OSIRIS-REx thermal emission spectrometer (OTES) instrument. Space Science Reviews, 214(5), 87.

Christoffersen, R., Rahman, Z., & Keller, L. P. (2012). Solar ion sputter deposition in the lunar regolith: experimental simulation using focused-ion beam techniques.

Clark, B. E., Fanale, F. P., & Salisbury, J. W. (1992). Meteorite-asteroid spectral comparison: The effects of comminution, melting, and recrystallization. *Icarus, 97*(2), 288-297.

Clark, B. E., Lucey, P., Helfenstein, P., Bell, J. F., Peterson, C., Veverka, J., ... & Izenberg, N. I. (2001). Space weathering on Eros: Constraints from albedo and spectral measurements of Psyche crater. *Meteoritics & Planetary Science*, 36(12), 1617-1637.

Clark, B. E., Hapke, B., Pieters, C., & Britt, D. (2002). Asteroid space weathering and regolith evolution. *Asteroids III*, 585, 90086-2.

Clark, B. E., Ziffer, J., Nesvorny, D., Campins, H., Rivkin, A. S., Hiroi, T., ... & DeMeo, F. (2010). Spectroscopy of B-type asteroids: Subgroups and meteorite analogs. *Journal of Geophysical Research: Planets*, 115(E6).

Conel, J. E., & Nash, D. B. (1970). Spectral reflectance and albedo of Apollo 11 lunar samples: Effects of irradiation and vitrification and comparison with telescopic observations. *Geochimica et Cosmochimica Acta Supplement*, 1, 2013.

De León, J., Campins, H., Morate, D., De Prá, M., Alí-Lagoa, V., Licandro, J., ... & Popescu, M. (2018). Expected spectral characteristics of (101955) Bennu and (162173) Ryugu, targets of the OSIRIS-REx and Hayabusa2 missions. *Icarus*, 313, 25-37.

DeMeo, F. E., Binzel, R. P., Slivan, S. M., & Bus, S. J. (2009). An extension of the Bus asteroid taxonomy into the near-infrared. *Icarus*, 202(1), 160-180.

Dukes, C. A., Baragiola, R. A., & McFadden, L. A. (1999). Surface modification of olivine by H+ and He+ bombardment. *Journal of Geophysical Research: Planets*, 104(E1), 1865-1872.

Fazio, A., Harries, D., Matthäus, G., Mutschke, H., Nolte, S., & Langenhorst, F. (2018). Femtosecond laser irradiation of olivine single crystals: Experimental simulation of space weathering. *Icarus*, 299, 240-252.

Fornasier, S., Lantz, C., Barucci, M. A., & Lazzarin, M. (2014). Aqueous alteration on main belt primitive asteroids: Results from visible spectroscopy. *Icarus, 233*, 163-178.

Fornasier, S., Lantz, C., Perna, D., Campins, H., Barucci, M. A., & Nesvorny, D. (2016). Spectral variability on primitive asteroids of the Themis and Beagle families: Space weathering effects or parent body heterogeneity?. *Icarus*, 269, 1-14.

Gaffey, M. J., Bell, J. F., Brown, R. H., Burbine, T. H., Piatek, J. L., Reed, K. L., & Chaky, D. A. (1993). Mineralogical variations within the S-type asteroid class. *Icarus, 106*(2), 573-602.

Gaffey, M. J. (2010). Space weathering and the interpretation of asteroid reflectance spectra. *Icarus*, 209(2), 564-574.

Gillis-Davis, J. J., Lucey, P. G., Bradley, J. P., Ishii, H. A., & Connolly, H. C. (2013, March). Laser space weathering of Allende meteorite. In *Lunar and Planetary Science Conference* (Vol. 44, p. 2494).

Gillis-Davis, J. J., Gasda, P. J., Bradley, J. P., Ishii, H. A., & Bussey, D. B. J. (2015, March). Laser space weathering of Allende (CV2) and Murchison (CM2) carbonaceous chondrites. In *Lunar and Planetary Science Conference* (Vol. 46, p. 1607).

Gillis-Davis, J. J., Lucey, P. G., Bradley, J. P., Ishii, H. A., Kaluna, H. M., Misra, A., & Connolly Jr, H. C. (2017). Incremental laser space weathering of Allende reveals non-lunar like space weathering effects. *Icarus*, 286, 1-14.

Gillis-Davis, J. J., Ishii, H. A., Adams, M., & Connolly, H. C. (2017, March). Laser irradiation of two CV3 meteorites yields desparate weathering effects. In *Lunar and Planetary Science Conference* (Vol. 48).

Gold, T. (1955). The lunar surface. *Monthly Notices of the Royal Astronomical Society, 115*(6), 585-604.

Gosling, J. T. (2014). The solar wind. In *Encyclopedia of the solar system* (pp. 261-279). Elsevier.

Hapke, B. (1965). Effects of a simulated solar wind on the photometric properties of rocks and powders. *Annals of the New York Academy of Sciences, 123*(2), 711-721.

Hapke, B. (1968). Lunar surface: Composition inferred from optical properties. *Science, 159*(3810), 76-79.

Hapke, B., Cassidy, W., & Wells, E. (1975). Effects of vapor-phase deposition processes on the optical, chemical, and magnetic properties OE the lunar regolith. *The moon*, 13(1-3), 339-353.

Hapke, B. (2001). Space weathering from Mercury to the asteroid belt. *Journal of Geophysical Research: Planets*, 106(E5), 10039-10073.

Hiroi, T., Pieters, C. M., Zolensky, M. E., & Lipschutz, M. E. (1993). Evidence of thermal metamorphism on the C, G, B, and F asteroids. *Science, 261*(5124), 1016-1018.

Hiroi, T., Sasaki, S., Misu, T., & Nakamura, T. (2013, March). Keys to detect space weathering on Vesta: changes of visible and near-infrared reflectance spectra of HEDs and carbonaceous chondrites. In *Lunar and Planetary Science Conference* (Vol. 44, p. 1276).

Ishiguro, M., Hiroi, T., Tholen, D. J., Sasaki, S., Ueda, Y., Nimura, T., ... & Nakamura, R. (2007). Global mapping of the degree of space weathering on asteroid 25143 Itokawa by Hayabusa/AMICA observations. *Meteoritics & Planetary Science*, 42(10), 1791-1800.

Jedicke, R., Nesvorný, D., Whiteley, R., Ivezić, Ž., & Jurić, M. (2004). An age–colour relationship for main-belt S-complex asteroids. *Nature*, 429(6989), 275-277.

Kaluna, H. M., Masiero, J. R., & Meech, K. J. (2016). Space weathering trends among carbonaceous asteroids. *Icarus*, 264, 62-71.

Kareev, M. S., Sears, D. W. G., Benoit, P. H., & Atabaev, B. G. (2003). The importance of solar wind in the production of "space weathering" features on the Moon and on asteroids. *LPI*, 1110.

Keller, L. P., & McKay, D. S. (1997). The nature and origin of rims on lunar soil grains. *Geochimica et Cosmochimica Acta*, 61(11), 2331-2341.

Keller, L. P., Christoffersen, R., Dukes, C. A., Baragiola, R. A., & Rahman, Z. (2015). Ion irradiation experiments on the Murchison CM2 carbonaceous chondrite: Simulating space weathering of primitive asteroids.

Kissel, J., & Krueger, F. R. (1987). Ion formation by impact of fast dust particles and comparison with related techniques. *Applied Physics A*, 42(1), 69-85.

Kitazato, K., Milliken, R. E., Iwata, T., Abe, M., Ohtake, M., Matsuura, S., ... & Senshu, H. (2019). The surface composition of asteroid 162173 Ryugu from Hayabusa2 near-infrared spectroscopy. *Science*, 364(6437), 272-275.

Landsman, Z. A., Emery, J. P., Campins, H., Hanuš, J., Lim, L. F., & Cruikshank, D. P. (2018). Asteroid (16) Psyche: Evidence for a silicate regolith from spitzer space telescope spectroscopy. Icarus, 304, 58-73.

Lantz, C., Clark, B. E., Barucci, M. A., & Lauretta, D. S. (2013). Evidence for the effects of space weathering spectral signatures on low albedo asteroids. *Astronomy & Astrophysics*, 554, A138.

Lantz, C., Brunetto, R., Barucci, M. A., Dartois, E., Duprat, J., Engrand, C., ... & Quirico, E. (2015). Ion irradiation of the Murchison meteorite: Visible to mid-infrared spectroscopic results. *Astronomy & Astrophysics*, 577, A41.

Lantz, C., Brunetto, R., Barucci, M. A., Bachelet, C., Baklouti, D., Bourçois, J., ... & Godard, M. (2015, October). Ion irradiation of carbonaceous chondrites as a simulation of space weathering on C-complex asteroids. In *European Planetary Science Congress 2015, held 27 September-2 October, 2015 in Nantes, France* (Vol. 10, pp. EPSC2015-138).

Lantz, C., Brunetto, R., Barucci, M. A., Fornasier, S., Baklouti, D., Bourçois, J., & Godard, M. (2017). Ion irradiation of carbonaceous chondrites: A new view of space weathering on primitive asteroids. *Icarus*, 285, 43-57.

Lantz, C., Binzel, R. P., & DeMeo, F. E. (2018). Space weathering trends on carbonaceous asteroids: A possible explanation for Bennu's blue slope?. *Icarus*, 302, 10-17.

Lantz, C., Brunetto, R., Baklouti, D., & Nakamura, T. (2019). More ion irradiated meteorites: expanding the space weathering view of dark asteroids. EPSC, 2019, EPSC-DPS2019.

Laul, J. C., & Papike, J. J. (1980). The lunar regolith-comparative chemistry of the Apollo sites. In *Lunar and Planetary Science Conference Proceedings* (Vol. 11, pp. 1307-1340).

Lauretta, D. S., Nagahara, H., & Alexander, C. M. D. (2006). Petrology and origin of ferromagnesian silicate chondrules. *Meteorites and the early solar system II*, 431-459.

Lazzarin, M., Marchi, S., Moroz, L. V., Brunetto, R., Magrin, S., Paolicchi, P., & Strazzulla, G. (2006). Space weathering in the main asteroid belt: The big picture. *The Astrophysical Journal Letters*, 647(2), L179.

Lim, L. F., McConnochie, T. H., Bell III, J. F., & Hayward, T. L. (2005). Thermal infrared (8–13 μm) spectra of 29 asteroids: the Cornell mid-infrared asteroid spectroscopy (MIDAS) survey. *Icarus, 173*(2), 385-408.

Loeffler, M. J., Dukes, C. A., & Baragiola, R. A. (2009). Irradiation of olivine by 4 keV He+: Simulation of space weathering by the solar wind. *Journal of Geophysical Research: Planets*, 114(E3).

Loeffler, M. J., Dukes, C. A., Christoffersen, R., & Baragiola, R. A. (2016). Space weathering of silicates simulated by successive laser irradiation: In situ reflectance measurements of Fo90, Fo99+, and SiO2. *Meteoritics & Planetary Science*, 51(2), 261-275.

Marchi, S., Brunetto, R., Magrin, S., Lazzarin, M., & Gandolfi, D. (2005). Space weathering of near-Earth and main belt silicate-rich asteroids: observations and ion irradiation experiments. *Astronomy & Astrophysics*, 443(3), 769-775.

Matsuoka, M., Nakamura, T., Kimura, Y., Hiroi, T., Nakamura, R., Okumura, S., & Sasaki, S. (2015). Pulse-laser irradiation experiments of Murchison CM2 chondrite for reproducing space weathering on C-type asteroids. *Icarus*, 254, 135-143.

Matsuoka, M., Nakamura, T., Kimura, Y., Hiroi, T., Nakamura, R., Okumura, S., & Sasaki, S. (2016, March). Reproducing space weathering on C-Type asteroids with low-energy laser irradiation experiments of the Murchison meteorite. In *Lunar and Planetary Science Conference* (Vol. 47, p. 1823).

Matsuoka, M., Nakamura, T., Hiroi, T., Kitazato, K., Iwata, T., Abe, M., ... & Matsuura, S. (2019, March). Infrared Spectra of Asteroid Ryugu: Comparison to Laboratory-Measured Carbonaceous Chondrites. In *Lunar and Planetary Science Conference* (Vol. 50).

Michel, P., DeMeo, F. E., & Bottke, W. F. (2015). Asteroids: recent advances and new perspectives. *Asteroids IV*, 1(3), 1.

Morota, T., Cho, Y., Kanamaru, M., Honda, R., Kameda, S., Tatsumi, E., ... & Sakatani, N. (2019, March). Timescale of reddening process of the Ryugu surface based on the crater size-frequency distribution. In *Lunar and Planetary Science Conference* (Vol. 50).

Morate, D., de León, J., De Prá, M., Licandro, J., Cabrera-Lavers, A., Campins, H., ... & Alí-Lagoa, V. (2016). Compositional study of asteroids in the Erigone collisional family using visible spectroscopy at the 10.4 m GTC. *Astronomy & Astrophysics, 586*, A129.

Morate, D., de León, J., De Prá, M., Licandro, J., Cabrera-Lavers, A., Campins, H., & Pinilla-Alonso, N. (2018). Visible spectroscopy of the Sulamitis and Clarissa primitive families: a possible link to Erigone and Polana. *Astronomy & Astrophysics, 610*, A25.

Moroz, L. V., Fisenko, A. V., Semjonova, L. F., Pieters, C. M., & Korotaeva, N. N. (1996). Optical effects of regolith processes on S-asteroids as simulated by laser shots on ordinary chondrite and other mafic materials. *Icarus*, 122(2), 366-382.

Moroz, L., Schade, U., & Wäsch, R. (2000). Reflectance spectra of olivine–orthopyroxene-bearing assemblages at decreased temperatures: Implications for remote sensing of asteroids. *Icarus*, 147(1), 79-93.

Moroz, L., Baratta, G., Strazzulla, G., Starukhina, L., Dotto, E., Barucci, M. A., ... & Distefano, E. (2004). Optical alteration of complex organics induced by ion irradiation: 1. Laboratory experiments suggest unusual space weathering trend. *Icarus*, 170(1), 214-228.

Moroz, L. V., Hiroi, T., Shingareva, T. V., Basilevsky, A. T., Fisenko, A. V., Semjonova, L. F., & Pieters, C. M. (2004, March). Reflectance spectra of CM2 chondrite Mighei irradiated with pulsed laser and implications for low-albedo asteroids and Martian moons. In *Lunar and Planetary Science Conference* (Vol. 35).

Morris, R. V., & Lauer Jr, H. V. (1980). The case against UV photostimulated oxidation of magnetite. *Geophysical Research Letters*, 7(8), 605-608.

Nakamura, T., Lantz, C., Kobayashi, S., Nakauchi, Y., Amano, K., Brurnetto, R., ... & Matsumoto, T. (2019, July). Experimental Reproduction of Space Weathering of C-Type Asteroids by He Exposure to Shocked and Partially Dehydrated Carbonaceous Chondrites. In *82nd Annual Meeting of The Meteoritical Society* (Vol. 2157).

Nash, D. B., Conel, J. E., & Greer, R. T. (1970). Luminescence and reflectance of tranquillity samples: Effects of irradiation and vitrification. *Science, 167*(3918), 721-724.

Nesvorný, D., Bottke, W. F., Vokrouhlický, D., Morbidelli, A., & Jedicke, R. (2005). Asteroid families. *Proceedings of the International Astronomical Union*, 1(S229), 289-299.

Nesvorný, D., Jedicke, R., Whiteley, R. J., & Ivezić, Ž. (2005). Evidence for asteroid space weathering from the Sloan Digital Sky Survey. *Icarus*, 173(1), 132-152.

Noble, S. K., Pieters, C. M., & Keller, L. P. (2007). An experimental approach to understanding the optical effects of space weathering. *Icarus*, 192(2), 629-642.

Noguchi, T., Nakamura, T., Kimura, M., Zolensky, M. E., Tanaka, M., Hashimoto, T., ... & Abe, M. (2011). Incipient space weathering observed on the surface of Itokawa dust particles. *Science, 333*(6046), 1121-1125.

Pieters, C. M., Fischer, E. M., Rode, O., & Basu, A. (1993). Optical effects of space weathering: The role of the finest fraction. *Journal of Geophysical Research: Planets*, 98(E11), 20817-20824.

Pieters, C. M., Taylor, L. A., Noble, S. K., Keller, L. P., Hapke, B., Morris, R. V., ... & Wentworth, S. (2000). Space weathering on airless bodies: Resolving a mystery with lunar samples. *Meteoritics & Planetary Science*, 35(5), 1101-1107.

Pizzarello, S., Cooper, G. W., & Flynn, G. J. (2006). The nature and distribution of the organic material in carbonaceous chondrites and interplanetary dust particles. *Meteorites and the early solar system II*, 1, 625-651.

Rivkin, A. S., Howell, E. S., Vilas, F., & Lebofsky, L. A. (2002). Hydrated minerals on asteroids: The astronomical record. *Asteroids III, 1*, 235-253.

Sasaki, S., Nakamura, K., Hamabe, Y., Kurahashi, E., & Hiroi, T. (2001). Production of iron nanoparticles by laser irradiation in a simulation of lunar-like space weathering. *Nature*, 410(6828), 555-557.

Sasaki, S., Hiroi, T., Nakamura, K., Hamabe, Y., Kurahashi, E., & Yamada, M. (2002). Simulation of space weathering by nanosecond pulse laser heating: Dependence on mineral composition, weathering trend of asteroids and discovery of nanophase iron particles. *Advances in Space Research*, 29(5), 783-788.

Shu, A., Collette, A., Drake, K., Grün, E., Horányi, M., Kempf, S., ... & Sternovsky, Z. (2012). 3 MV hypervelocity dust accelerator at the Colorado Center for Lunar Dust and Atmospheric Studies. Review of Scientific Instruments, 83(7), 075108.

Sugita, S., Honda, R., Morota, T., Kameda, S., Sawada, H., Tatsumi, E., ... & Sakatani, N. (2019). The geomorphology, color, and thermal properties of Ryugu: Implications for parent-body processes. *Science*, 364(6437), 252.

Sunshine, J. M., Connolly, H. C., McCoy, T. J., Bus, S. J., & La Croix, L. M. (2008). Ancient asteroids enriched in refractory inclusions. *Science, 320*(5875), 514-517.

Takir, D., Howard, K., Yabuta, H., McAdam, M., Hibbitts, C., & Emery, J. (2018). Linking water-rich asteroids and meteorites: implications for asteroid space missions. In *Primitive meteorites and asteroids* (pp. 371-408). Elsevier.

Taylor, L. A., Pieters, C. M., Keller, L. P., Morris, R. V., & McKay, D. S. (2001). Lunar mare soils: Space weathering and the major effects of surface-correlated nanophase Fe. *Journal of Geophysical Research: Planets*, 106(E11), 27985-27999.

Takir, D., Emery, J. P., Mcsween Jr, H. Y., Hibbitts, C. A., Clark, R. N., Pearson, N., & Wang, A. (2013). Nature and degree of aqueous alteration in CM and CI carbonaceous chondrites. *Meteoritics & Planetary Science, 48(*9), 1618-1637.

Tholen, D. J. (1984). Asteroid taxonomy from cluster analysis of photometry.

Tholen, D. J., & Barucci, M. A. (1989). Asteroid taxonomy. *aste*, 298-315.

Thompson, M. S., Christoffersen, R., Zega, T. J., & Keller, L. P. (2014). Micro-chemical and structural evidence for space weathering in soils from asteroid Itokawa. *Earth, Planets and Space*, 66(1), 1-10.

Thompson, M. S., Zega, T. J., Becerra, P., Keane, J. T., & Byrne, S. (2016). The oxidation state of nanophase Fe particles in lunar soil: Implications for space weathering. *Meteoritics & Planetary Science*, 51(6), 1082-1095.

Thompson, M. S., Zega, T. J., & Howe, J. Y. (2017). In situ experimental formation and growth of Fe nanoparticles and vesicles in lunar soil. *Meteoritics & Planetary Science*, 52(3), 413-427.

Thompson, M. S., Loeffler, M. J., Morris, R. V., Keller, L. P., & Christoffersen, R. (2019). Spectral and chemical effects of simulated space weathering of the Murchison CM2 carbonaceous chondrite. *Icarus*, 319, 499-511.

Tsuda, Y., Yoshikawa, M., Watanabe, S., Nakazawa, S., Terui, F., Saiki, T., ... & Kitazato, K. (2019, March). Hayabusa2 Mission Up to Now. In *Lunar and Planetary Science Conference* (Vol. 50).

Vernazza, P., Binzel, R. P., Rossi, A., Fulchignoni, M., & Birlan, M. (2009). Solar wind as the origin of rapid reddening of asteroid surfaces. *Nature*, 458(7241), 993-995.

Vernazza, P., Fulvio, D., Brunetto, R., Emery, J. P., Dukes, C. A., Cipriani, F., ... & Baragiola, R. A. (2013). Paucity of Tagish Lake-like parent bodies in the Asteroid Belt and among Jupiter Trojans. *Icarus*, 225(1), 517-525.

Vilas, F., & Gaffey, M. J. (1989). Phyllosilicate absorption features in main-belt and outer-belt asteroid reflectance spectra. *Science, 246*(4931), 790-792.

Vilas, F. (1994). A cheaper, faster, better way to detect water of hydration on Solar System bodies. *Icarus, 111*(2), 456-467.

Watanabe, S., Hirabayashi, M., Hirata, N., Hirata, N., Noguchi, R., Shimaki, Y., ... & Yabuta, H. (2019). Hayabusa2 arrives at the carbonaceous asteroid 162173 Ryugu—A spinning top–shaped rubble pile. *Science*, 364(6437), 268-272.

Weber, I., Stojic, A. N., Morlok, A., Reitze, M. P., Markus, K., Hiesinger, H., ... & Hübers, H. W. (2020). Space weathering by simulated micrometeorite bombardment on natural olivine and pyroxene: A coordinated IR and TEM study. Earth and Planetary Science Letters, 530, 115884.

Weisberg, M. K., McCoy, T. J., & Krot, A. N. (2006). Systematics and evaluation of meteorite classification. *Meteorites and the early solar system II.*

Young, C. L., Wray, J. J., Poston, M., Hand, K. P., & Carlson, R. W. (2017). The mid-IR spectral effects of darkening agents and porosity on the silicate surface features of airless bodies. AGUFM, 2017, P54B-07.

Ziffer, J., Campins, H., Licandro, J., Walker, M. E., Fernandez, Y., Clark, B. E., ... & Deshpande, R. (2011). Near-infrared spectroscopy of primitive asteroid families. *Icarus*, 213(2), 538-546.